






Contents lists available at ScienceDirect

European Journal of Mechanics / A Solids

journal homepage: www.elsevier.com/locate/ejmsol

Full Length Article

Enhancing bending and compression resistance of additively manufactured bio-inspired architected structures

Alessia Senatore^a, Mattia Venza^a, Sara Candidori^a , Serena Graziosi^a ,
Federica Buccino^{a,b,*} 

^a Politecnico di Milano, Department of Mechanical Engineering, 20156, Italy^b IRCCS Orthopedic Institute Galeazzi, Milan, Italy

ARTICLE INFO

Keywords:

Bio-inspired
Multi-axial loadbearing structures
Multi-objective optimization
Lightweight
Additive manufacturing

ABSTRACT

To tackle the challenge of optimizing structural performance and minimizing weight, this research explores the potential of multi-scale bio-inspired design principles in combination with 3D printing. Besides, multi-objective genetic algorithm-based optimization strategies are applied to enhance structure bending and compression resistance. Hollow cylinders, commonly used in piping, structural supports, and biomedical implants, are ideal for this approach as reducing their weight often compromises stiffness and stability, highlighting the need for new design strategies. Herein, the successful combination of bio-inspiration, including plant- and animal-based solutions, and multi-objective optimization plays a core role in the architected structure design to minimize volume and maximize reaction force. Among the various bio-inspired models evaluated, the *Horsetail* structure has emerged as the most effective, demonstrating 100% increase in the reaction force under bending loads, a 40% improvement in maximum displacement before instability, and a 20% increase in compressive resistance if compared to the reference hollow cylinder. Validation through a combined experimental and numerical approach confirms the accuracy and reliability of the developed models. The successful application of the Material Extrusion process to fabricate these bio-inspired structures proves their practical feasibility. Here, integrating these optimized designs into real-world applications can replace conventional cylindrical pylons with lighter, load-optimized 3D-printed alternatives.

1. Introduction

Optimizing structures to withstand combined loads while maintaining minimal weight remains a critical and evolving challenge in mechanical, biomedical, and aeronautical engineering (Ravi-Chandar, 2011). Historically, optimization approaches have progressed from the purely analytical methods of the nineteenth century to the contemporary combined numerical-experimental techniques (Yin et al., 2019). Despite significant advances, current methods often fail to address the complex interplay between structural efficiency and multi-load resistance (Sullivan et al., 2017; Buccino et al., 2022a). In such a context, bio-inspiration has already been demonstrated to be a promising strategy, where natural designs serve as a source of innovation (Zappa et al., 2024; Wang and Li, 2020; Buccino et al., 2021a). Over millions of years, Nature has perfected lightweight, optimized structures capable of withstanding diverse loads through hierarchical and tailored solutions (Yin et al., 2019; Khoshgoftar et al., 2022; Mirzaali et al., 2017).

Examples include bones and bamboo, which exhibit remarkable mechanical properties despite being composed of materials with relatively modest intrinsic properties (Libonati et al., 2020; Bru et al., 2020; Wegst and Ashby, 2004; Mirzaali et al., 2018; Libonati and Vergani, 2014; Buccino et al., 2022b). However, the full potential of these bio-inspired materials/structures has remained underexplored for years in the engineering community due to the challenges related to the design and manufacturing of such complex designs (Qu et al., 2024; Zhou et al., 2024; Shi et al., 2024; Xiong et al., 2023).

The rapid diffusion and advancements in manufacturing technologies, such as Additive Manufacturing (AM), have changed this scenario by facilitating the application of bio-inspired designs (Rohde et al., 2018; Niknam and Akbarzadeh, 2020; du Plessis et al., 2019). These technologies enable the fabrication of complex shapes previously unattainable with conventional approaches. AM, for instance, allows for precise control over material distribution and internal architecture, making it possible to replicate the intricate designs found in Nature

* Corresponding author. Via La Masa 1, 20156, Milano, Italy.

E-mail address: federica.buccino@polimi.it (F. Buccino).

<https://doi.org/10.1016/j.euomechsol.2024.105557>

Received 4 October 2024; Received in revised form 6 December 2024; Accepted 28 December 2024

Available online 31 December 2024

0997-7538/© 2024 The Authors. Published by Elsevier Masson SAS. This is an open access article under the CC BY-NC-ND license (<http://creativecommons.org/licenses/by-nc-nd/4.0/>).

(Maconachie et al., 2019; Mirzaali et al., 2020; Tran et al., 2017). Despite these capabilities, current manufacturing techniques still fail to fully exploit the potential of bio-inspired designs due to constraints in material properties and fabrication precision (Mirzaali et al., 2020). This gap between potential and practice underscores the importance of continued exploration into bio-inspired additively manufactured structures.

Architected materials, characterized by their periodic or non-periodic arrangements of unit cells, are a specific class of materials that have shown great potential in various engineering applications (Mueller et al., 2018). These materials can be designed to exhibit unique properties, such as high stiffness-to-weight ratios, enhanced energy absorption (Ha et al., 2023, 2024), and tailored deformation behavior (Saldívar et al., 2023). By mimicking the hierarchical structures found in nature, such as the multi-scale architecture of bone, the segmented design of bamboo, or the structure of a specific sea sponge, engineered architected materials can achieve performances that surpass those of conventional homogeneous materials (Yaraghi et al., 2016; Saldívar et al., 2022) or those of already existing architected materials (Mistry et al., 2023).

However, the current state of the art lacks comprehensive studies that 1) integrate nature-inspired features into conventional engineering applications or designs to analyze their potential structural contribution and 2) analyze the behavior of such bio-inspired structures in complex loading conditions. To address that lack, this study started by considering the hollow cylinder model as a structural reference due to its widespread use in multiple engineering applications. Indeed, due to their manufacturability and lightweight characteristics, hollow cylinders are commonly employed in piping, as structural supports, and in biomedical implants (i.e., transtibial prosthesis pylon) (Yin et al., 2019; Powelson and Yang, 2011; Tavangarian et al., 2019; Gao et al., 2016; Chen et al., 2017; Buccino et al., 2022c). However, their performance under multiple loading conditions, such as bending and compression, is often suboptimal (Tavangarian et al., 2019). Efforts to reduce the weight of these structures frequently encounter issues of reduced stiffness and instability (Li et al., 2022), underscoring the need for innovative solutions (Tavangarian et al., 2019; Lindberg et al., 2018; De Vivo Nicoloso et al., 2021). Therefore, while traditionally optimized for torsional loads, hollow cylinders present significant opportunities for improvement when subjected to combined loading scenarios.

Hence, this research focuses on enhancing hollow cylinders' combined bending and compression resistance by integrating bio-inspired multi-level architectures into their conventional design. By drawing inspiration from natural models such as the stems of bamboo and horsetail, the structure of DNA molecules, and the cuticle of arthropods, this study aims to incorporate hierarchical and architected configurations into a standard hollow cylinder design. These natural structures provide exceptional mechanical properties through their intricate internal architectures, which can be emulated to achieve superior performance in engineering applications.

To reach this goal, the research employs a bio-inspired multi-objective parametric optimization approach based on a genetic algorithm involving fine-tuning the geometrical dimensions of bio-inspired features, such as the thickness, spacing, and orientation of reinforcing elements, to achieve the desired mechanical performance. Numerical methods and simulations are used to analyze the mechanical behavior of these optimized structures, comparing them to traditional hollow cylinders with equivalent volumes. Additionally, experimental validation is conducted using 3D-printed samples fabricated with the Fused Filament Fabrication (FFF) technology. This ensures the optimized designs perform as expected under real-world conditions, bridging the gap between theoretical predictions and practical applications. Besides, the Material Extrusion (MEX) process also offers the potential to scale the developed configurations. Ultimately, this research aims to straighten the relevance of nature-inspired additively manufactured architected solutions in the material and engineering fields because they can lead to

groundbreaking improvements in structural performance without compromising manufacturing efficiency.

2. Materials and methods

2.1. Bio-inspired architected structure design

2.1.1. The bio-inspirational sources

Fayemi et al. (2017) and Katiyar et al. (Katiyar et al., 2021; Buccino et al., 2021b) have delineated a methodical approach to bioinspired design articulated through eight steps, advocating a structured, problem-driven process. In this study, that methodology has been applied as follows (Fig. 1A).

1. *Problem analysis*: the need to enhance the bending and compressive response of hollow cylindrical structures, commonly used but with suboptimal performance.
2. *Problem abstraction*: increasing stiffness and strength of hollow cylindrical structures under bending conditions and improving their maximum displacement and force before buckling under quasi-static compressive conditions.
3. *Transposition to biology*: analyzing how natural organisms resist bending and compressive loads.
4. *Identification of potential biological models*: Bamboo cells, horsetail, DNA structures, and bamboo nodes have emerged as promising inspirations based on a review of relevant studies in the field.
5. *Selection of biological models*: narrowing down the identified bio-inspired structures to those most applicable for the selected design (i.e., the hollow cylinder).
6. *Abstraction of biological strategies*: determining which features of the biological source are suitable for solving the design problem.
7. *Transposition to technology*: assessing the technical feasibility of the chosen biological solution/model and identifying potential technologies for implementation.
8. *Implementation in the initial context*: generating and validating the bioinspired design numerically and experimentally.

Concerning step 4, as anticipated, the following bio-inspirational sources (and a combination of them) have been considered in designing the structures to improve the bending and compression resistance of hollow structures: bamboo, horsetail, DNA, and arthropod exoskeletons, each chosen for its exceptional structural features and performance under stress. Their use has been inspired by the relevant literature in the field, as explained hereafter.

Bamboo is renowned for its rapid growth and remarkable strength-to-weight ratio. Its stem *macrostructure*, characterized by a woody circular hollow column with periodic nodes and internal diaphragms, provides a model for creating structures that resist bending and buckling (Chen et al., 2018; Osorio et al., 2018; Amada et al., 1997; Umer et al., 2014; Wegst, 2011). The stem wall's *microstructure*, with its radial distribution of dense and sparse zones, vascular bundles, and *parenchyma* cells, offers insights into material optimization (Wegst, 2011; Svatík et al., 2021). Bamboo's modulus of elasticity ranges between 20 and 40 GPa, and its ultimate tensile strength can reach up to 300 MPa (Tan et al., 2011). In structure design, bamboo's macrostructure inspired the generation of hollow cylindrical structures reinforced with periodic external rings and internal diaphragms, mimicking bamboo's nodes (Taylor et al., 2015) and diaphragms to enhance stiffness and strength without adding significant weight.

Horsetail plants, particularly their hollow, jointed, ridged stems, inspired the design of structures with internal walls connected by radial ribs extending along the cylinder's length (Yin et al., 2015, 2016; Xiao et al., 2016). This design aims to reduce weight while increasing pressure resistance and bending stiffness, emulating the pillar-like structure found in horsetail stems. Horsetail stems exhibit a modulus of elasticity around 10 GPa: including a gradient in porosity, and the geometric

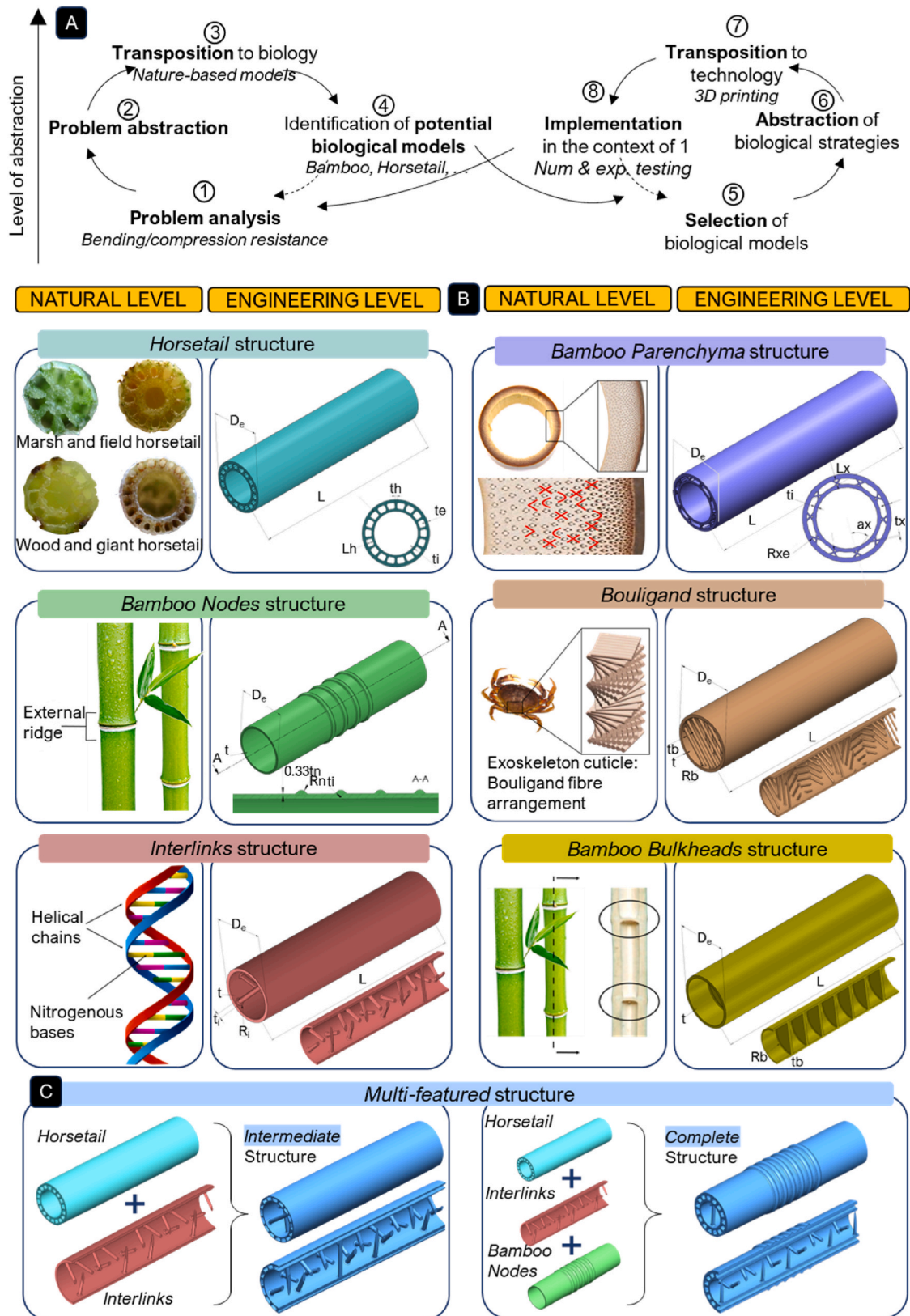


Fig. 1. Bio-inspired architected structure methodological approach and design. **A.** Methodological approach employed for the design of compression- and bending-resistant bio-inspired structures. **B.** Bio-inspired design implementation: for each structure, it is reported the natural source of inspiration and its translation to an engineered design. Six architectures are considered: *Horsetail*, *Bamboo Parenchyma*, *Bamboo Nodes*, *Bouligand*, *Interlinks*, and *Bamboo Bulkheads*, taking inspiration from plant multi-scale design, arthropod cuticle, and DNA inner architectures. For the sake of comparison, all bio-inspired structures exhibit the same external diameter $D_e = 30$ mm and length $L = 120$ mm. **C.** Multi-featured architected structures, as a combination of *Horsetail*, *Interlinks* (*Intermediate structure*), and *Bamboo Nodes* (*Complete structure*).

Table 1
Overview of the considered bio-inspired structures. The considered wall thickness (t) is 1.5 mm.

Bio-inspired structure type (natural inspiration)	Varied parameters	Numerical tests	Experimental tests
Single-featured bio-inspired structures			
Horsetail (inspired by Horsetail plants)	Rib thickness (th) [0.4–1.6 mm] Rib number (Zappa et al., 2024; Wang and Li, 2020; Buccino et al., 2021a; Khoshgoftar et al., 2022; Mirzaali et al., 2017; Libonati et al., 2020; Bru et al., 2020; Wegst and Ashby, 2004; Mirzaali et al., 2018; Libonati and Vergani, 2014; Buccino et al., 2022b; Qu et al., 2024; Zhou et al., 2024; Shi et al., 2024; Xiong et al., 2023; Rohde et al., 2018; Niknam and Akbarzadeh, 2020; du Plessis et al., 2019; Maconachie et al., 2019; Mirzaali et al., 2020; Tran et al., 2017; Mueller et al., 2018; Ha et al., 2024; Ha et al., 2023; Saldívar et al., 2023; Yaraghi et al., 2016; Saldívar et al., 2022; Mistry et al., 2023; Powelson and Yang, 2011; Tavangarian et al., 2019; Gao et al., 2016)	Four-point bending Compression	Four-point bending (three replicas of the optimized structure) Compression (three replicas of the optimized structure)
Bamboo Parenchyma (inspired by Bamboo microstructure)	Rib length (Lh) [1–3.5 mm] Rib thickness (tx) [0.2–0.6 mm] Rib number (Zappa et al., 2024; Wang and Li, 2020; Buccino et al., 2021a, 2022b; Khoshgoftar et al., 2022; Mirzaali et al., 2017, 2018; Libonati et al., 2020; Bru et al., 2020; Wegst and Ashby, 2004; Libonati and Vergani, 2014; Qu et al., 2024; Zhou et al., 2024; Shi et al., 2024; Xiong et al., 2023; Rohde et al., 2018)	Four-point bending	
Bamboo Nodes (inspired by Bamboo macrostructure)	Rib length (Lx) [1.5–2.5 mm] Rib angle (ax) [30–55°] Ridges radius (Rn) [1–2 mm] Ridges number (Sullivan et al., 2017; Buccino et al., 2022a; Zappa et al., 2024; Wang and Li, 2020)	Four-point bending Compression Four-point bending	Compression (three replicas of the optimized structure)
Bouligand (inspired by arthropod exoskeleton)	Strut thickness (tb) [1.0–2.5 mm] Strut number per layer (Sullivan et al., 2017; Buccino et al., 2021a, 2022a; Zappa et al., 2024; Wang and Li, 2020; Khoshgoftar et al., 2022; Mirzaali et al., 2017) Layer number (Wang and Li, 2020; Buccino et al., 2021a, 2022b; Khoshgoftar et al., 2022; Mirzaali et al., 2017, 2018; Libonati et al., 2020; Bru et al., 2020; Wegst and Ashby, 2004; Libonati and Vergani, 2014; Qu et al., 2024; Zhou et al., 2024; Shi et al., 2024)	Four-point bending	
Interlinks (inspired by DNA struts)	Strut thickness (ti) [1.0–2.5 mm] Struct number (Mirzaali et al., 2017; Libonati et al., 2020; Bru et al., 2020; Wegst and Ashby, 2004; Mirzaali et al., 2018; Libonati and Vergani, 2014; Buccino et al., 2022b; Qu et al., 2024; Zhou et al., 2024; Shi et al., 2024; Xiong et al., 2023; Rohde et al., 2018; Niknam and Akbarzadeh, 2020; du Plessis et al., 2019; Maconachie et al., 2019; Mirzaali et al., 2020; Tran et al., 2017; Mueller et al., 2018; Ha et al., 2024; Ha et al., 2023; Saldívar et al., 2023; Yaraghi et al., 2016; Saldívar et al., 2022; Mistry et al., 2023; Powelson and Yang, 2011; Tavangarian et al., 2019; Gao et al., 2016; Chen et al., 2017; Buccino et al., 2022c; Li et al., 2022; Lindberg et al., 2018; De Vivo Nicoloso et al., 2021; Fayemi et al., 2017; Katiyar et al., 2021; Buccino et al., 2021b; Chen et al., 2018; Osorio et al., 2018; Amada et al., 1997; Umer et al., 2014; Wegst, 2011; Svatk et al., 2021)	Four-point bending Compression	Compression (three replicas of the optimized structure)
Bamboo bulkhead (inspired by Bamboo macrostructure)	Bulkhead thickness (tb) [0.75–2.0 mm] Bulkhead number (Yin et al., 2019; Sullivan et al., 2017; Buccino et al., 2021a, 2022a; Zappa et al., 2024; Wang and Li, 2020)	Four-point bending	
Multi-featured bio-inspired structures			
Intermediate	Rib thickness [0.4–1.6 mm] Rib number (Zappa et al., 2024; Wang and Li, 2020; Buccino et al., 2021a; Khoshgoftar et al., 2022; Mirzaali et al., 2017; Libonati et al., 2020; Bru et al., 2020; Wegst and Ashby, 2004; Mirzaali et al., 2018; Libonati and Vergani, 2014; Buccino et al., 2022b; Qu et al., 2024; Zhou et al., 2024; Shi et al., 2024; Xiong et al., 2023; Rohde et al., 2018; Niknam and Akbarzadeh, 2020; du Plessis et al., 2019; Maconachie et al., 2019; Mirzaali et al., 2020; Tran et al., 2017; Mueller et al., 2018; Ha et al., 2024; Ha et al., 2023; Saldívar et al., 2023; Yaraghi et al., 2016; Saldívar et al., 2022; Mistry et al., 2023; Powelson and Yang, 2011; Tavangarian et al., 2019; Gao et al., 2016; Chen et al., 2017; Buccino et al., 2022c; Li et al., 2022; Lindberg et al., 2018; De Vivo Nicoloso et al., 2021; Fayemi et al., 2017; Katiyar et al., 2021; Buccino et al., 2021b; Chen et al., 2018; Osorio et al., 2018; Amada et al., 1997; Umer et al., 2014; Wegst, 2011; Svatk et al., 2021) Rib length [1–3.5 mm] Strut thickness [1.0–2.5 mm] Struct number (Mirzaali et al., 2017; Libonati et al., 2020; Bru et al., 2020; Wegst and Ashby, 2004; Mirzaali et al., 2018; Libonati and Vergani, 2014; Buccino et al., 2022b; Qu et al., 2024; Zhou et al., 2024; Shi et al., 2024; Xiong et al., 2023; Rohde et al., 2018; Niknam and Akbarzadeh, 2020; du Plessis et al., 2019; Maconachie et al., 2019; Mirzaali et al., 2020; Tran et al., 2017; Mueller et al., 2018; Ha et al., 2024; Ha et al., 2023; Saldívar et al., 2023; Yaraghi et al., 2016; Saldívar et al., 2022; Mistry et al., 2023; Powelson and Yang, 2011; Tavangarian et al., 2019; Gao et al., 2016; Chen et al., 2017; Buccino et al., 2022c; Li et al., 2022; Lindberg et al., 2018; De Vivo Nicoloso et al., 2021; Fayemi et al., 2017; Katiyar et al., 2021; Buccino et al., 2021b; Chen et al., 2018; Osorio et al., 2018; Amada et al., 1997; Umer et al., 2014; Wegst, 2011; Svatk et al., 2021)	Four-point bending	
Complete	Rib thickness [0.4–1.6 mm] Rib number (Zappa et al., 2024; Wang and Li, 2020; Buccino et al., 2021a; Khoshgoftar et al., 2022; Mirzaali et al., 2017; Libonati et al., 2020; Bru et al., 2020; Wegst and Ashby, 2004; Mirzaali et al., 2018; Libonati and Vergani, 2014; Buccino et al., 2022b; Qu et al., 2024; Zhou et al., 2024; Shi et al., 2024; Xiong et al., 2023;	Compression	Compression (three replicas)

(continued on next page)

Table 1 (continued)

Bio-inspired structure type (natural inspiration)	Varied parameters	Numerical tests	Experimental tests
	<p>Rohde et al., 2018; Niknam and Akbarzadeh, 2020; du Plessis et al., 2019; Maconachie et al., 2019; Mirzaali et al., 2020; Tran et al., 2017; Mueller et al., 2018; Ha et al., 2024; Ha et al., 2023; Saldívar et al., 2023; Yaraghi et al., 2016; Saldívar et al., 2022; Mistry et al., 2023; Powelson and Yang, 2011; Tavangarian et al., 2019; Gao et al., 2016)</p> <p>Rib length [1–3.5 mm]</p> <p>Strut thickness [1.0–2.5 mm]</p> <p>Strut number (Mirzaali et al., 2017; Libonati et al., 2020; Bru et al., 2020; Wegst and Ashby, 2004; Mirzaali et al., 2018; Libonati and Vergani, 2014; Buccino et al., 2022b; Qu et al., 2024; Zhou et al., 2024; Shi et al., 2024; Xiong et al., 2023; Rohde et al., 2018; Niknam and Akbarzadeh, 2020; du Plessis et al., 2019; Maconachie et al., 2019; Mirzaali et al., 2020; Tran et al., 2017; Mueller et al., 2018; Ha et al., 2024; Ha et al., 2023; Saldívar et al., 2023; Yaraghi et al., 2016; Saldívar et al., 2022; Mistry et al., 2023; Powelson and Yang, 2011; Tavangarian et al., 2019; Gao et al., 2016; Chen et al., 2017; Buccino et al., 2022c; Li et al., 2022; Lindberg et al., 2018; De Vivo Nicoloso et al., 2021; Fayemi et al., 2017; Katiyar et al., 2021; Buccino et al., 2021b; Chen et al., 2018; Osorio et al., 2018; Amada et al., 1997; Umer et al., 2014; Wegst, 2011; Svatk et al., 2021)</p> <p>Ridges radius [1–2 mm]</p> <p>Ridges number (Sullivan et al., 2017; Buccino et al., 2022a; Zappa et al., 2024; Wang and Li, 2020)</p>		

arrangement of the ribs is thought to contribute to a lightweight yet strong design (Yin et al., 2016).

DNA provides inspiration through its double-helix structure, characterized by interconnected antiparallel chains of nucleotides. This helical arrangement offers a model for creating resilient structures capable of distributing stress evenly. DNA's helical pitch ranges between 2.5 and 3.5 nm. In structure design, DNA's helical pattern is mimicked by adding circular-shaped struts, i.e. interlinks, in an antiparallel helical pattern to reinforce the cylindrical walls (Zheng et al., 2019). This design enhances the structure's ability to withstand bending and compressive forces while maintaining flexibility and strength.

Arthropod exoskeletons, specifically the endocuticle with its Bouligand structure, which has a tensile strength of up to 150 MPa and an elastic modulus of around 6 GPa, offer insights into designing impact-resistant materials (Bouligand, 1972; Moïni et al., 2018; Porter et al., 2015; Ginzburg et al., 2017). The helical arrangement of chitin fibers in the exoskeleton provides a model for developing structures that can absorb and dissipate energy efficiently.

These natural systems and their distinguishing features are uniquely combined in this work for the design of bending and compression-resistant engineered solutions.

2.1.2. Design implementation

The design phase has aimed to generate bio-mimetic thin-walled cylindrical structures with enhanced flexural and compressive behaviors compared to conventional cylinders. In Fig. 1B, all the developed bio-inspired designs are shown by comparing the engineered solution with the natural one. To demonstrate these improved performances, a reference hollow cylinder with fixed parameters—30 mm external diameter and 120 mm length (90 mm for compressive tests)—was set as a baseline for comparison. Its wall thickness was varied to maintain consistent volume across the various tested bio-inspired configurations reported in Table 1. Specifically, reference hollow cylinders with thicknesses ranging from 1 mm to 4.5 mm (with 0.25 mm increase, so a total of 15 reference cylinders) were generated to produce a reference regression curve correlating reaction force to volume.

The first bio-inspired structure (**Horsetail** structure, Fig. 1B) design is based on the horsetail plant's (*Equisetum*) evolutionary adaptations to withstand bending forces despite its slender form. This plant thrives in environments with high wind or mechanical stresses, thanks to its internal wall supported by radial ribs that extend outward. These ribs help distribute external forces, preventing bending failure while maintaining the plant's lightweight and flexible nature. Evolved to survive in open

environments like grasslands or coastal areas, the horsetail plant structure provides an efficient balance of strength and flexibility. In our design, the fixed parameters—outer diameter, length, and inner wall thickness (0.75 times the outer wall)—mimic the plant's structural consistency, while the adjustable rib dimensions (thickness, number of ribs, and length) optimize bending resistance and material efficiency. The second bamboo parenchyma-inspired structure (**Bamboo Parenchyma** structure, Fig. 1B) employs concentric thin-walled cylinders connected by X-shaped ribs in a circular pattern, optimizing the distribution of mechanical stresses. This configuration abstracts the functional principles of bamboo parenchyma, where radial gradients in dense and porous regions efficiently distribute mechanical stresses. In bamboo, the parenchyma's microstructural organization optimizes the strength-to-weight ratio by combining stiff vascular bundles with softer, porous tissue, allowing for efficient load distribution and flexibility. Variable parameters include rib dimensions (thickness, number of ribs, length) and opening angles, with inner wall thickness set at 0.75 times the outer wall. The third bamboo-inspired design (**Bamboo Nodes** structure, Fig. 1B) mimicked the plant's macrostructure by incorporating external ridges (variable parameters include ridges radius and number) to reinforce the cylindrical wall, targeting enhanced resistance to buckling and compressive forces. The fourth structure draws inspiration from the Bouligand helix found in arthropod exoskeletons (**Bouligand** structure, Fig. 1B), incorporating helicoidally arranged internal struts to improve impact resistance and energy dissipation. Design parameters such as strut number, thickness, and number of layers are varied while maintaining constant cylinder dimensions. The fifth structure, inspired by DNA's double-helix (**Interlinks** structure, Fig. 1B), exploits antiparallel helical struts to reinforce the cylinder, enhancing flexibility and compressive strength via interlinks. Parameters included the number of struts and their thickness, with modifications for manufacturability considerations in 3D printing. Finally, the sixth bamboo bulkhead-inspired structure (**Bamboo bulkhead** structure, Fig. 1B) features internal diaphragms mimicking the plant's internal structure, designed to distribute loads evenly across the cylinder's cross-section. Variable features include bulkhead thickness and number.

In addition to the previous configurations, **multi-featured structures** (Fig. 1C) are also generated by combining the most promising features from the single-featured designs (Fig. 1B). They integrate elements such as horsetail-inspired radial ribs, DNA-like helical struts, and bamboo nodes' external rings (Fig. 1C). The difference between the **Complete** (Fig. 1C, right) and the **Intermediate** (Fig. 1C, left) structure is that the first also incorporates the **Bamboo Nodes** feature (Fig. 1B).

2.2. Bio-inspired structure manufacturing

The designed bio-inspired structures are manufactured using the Ultimaker S3, a state-of-the-art FFF 3D printer. The structures are designed using *Solidworks 2021*, then converted to STL files and processed through Ultimaker Cura software to generate the necessary G-code for printing. The Ultimaker Polypropylene (PP) is chosen for its favorable mechanical properties, such as a tensile modulus of 220 MPa and strain at break greater than 300%, which are essential for testing the performance of the bio-inspired structures under various loading conditions. The material properties have been extrapolated from tensile and compressive experimental tests and are reported in [Appendix A.1](#).

For both compression and the four-point bending tests, the chosen printing direction is parallel to the vertical axis of the cylindrical wall; this choice guarantees better results in terms of surface finishing and geometrical feature realization. Four replicas were printed for each configuration to be tested under compression, and three replicas each for the four-point bending tests. Printing parameters include 0.2 mm layer height, 0.38 mm line width, 100% infill density, zig-zag infill pattern, and 25 mm/s print speed.

2.3. Experimental testing

The MTS Alliance RF/150 machine, capable of applying up to 150 kN of force, is employed to assess how these structures perform under compressive loads. Each sample is accurately positioned on the machine's compression plates, with attention to centering to avoid alignment errors. A digital extensometer records displacement up to 1 mm while the testing adheres to ASTM [D695](#) standards, applying a constant displacement rate of 1.3 mm/min (in the direction of the cylinder axis) until the specimen exhibits instability. The data collected from these tests, including force and displacement, are used to construct stress-strain curves, shedding light on the structural integrity and deformation behavior of the bio-inspired designs.

The MTS Synergie 200, equipped with a specialized four-point bending system and custom-designed supports to mitigate issues like sliding and surface damage, is used for flexural tests. The setup includes a preload of 300 N to stabilize the samples, with the machine moving the crosshead at a controlled speed of 1 mm/min until a displacement of 3 mm is reached. This approach ensures a thorough evaluation of the bending performance, with load-displacement curves derived from the data serving to validate numerical models and assess the structural response.

2.4. Numerical analyses

The numerical analyses for the bio-inspired architected structures exploit ABAQUS/CAE 2017 software to perform detailed finite element analyses (FEA) for both four-point bending and compression tests.

The four-point bending test involves importing the structure as 3D deformable parts and generating rigid 3D shell pins with a 10 mm diameter and 25 mm length. Material properties are set based on Ultimaker PP data, with Young's modulus (E) at 220 MPa and Poisson's ratio (ν) at 0.43 ([Ultimaker and Ultimaker PP Technical Datasheet, 2022](#)). The assembly includes setting loading spans of 50 mm and support spans of 100 mm and employing a general static step with the *Nlgeom* option enabled to capture non-linear behavior. Boundary conditions are applied where supporting pins are fully encastered and loading pins constrained to move only vertically, with a displacement-controlled load of 1 mm downward. Convergence analysis involves varying mesh sizes from 1 mm to 3.5 mm, focusing on Reaction Force (RF) and Von Mises stress to ensure accuracy within 2% and 6% thresholds, respectively.

Structures are imported as 3D deformable parts for the compression test, and rigid 3D shell plates are generated with a 40 mm side. The material properties are defined using a true stress-strain curve derived

Table 2

Horsetail, Interlinks, and Bamboo Nodes Sobol' sequence geometrical constraints.

<i>Horsetail</i>	Thickness (th) [mm]	Number [-]	Length (Lh) [mm]	Wall thickness (t) [mm]
Minimum	0.4	5	1	0.8
Maximum	1.6	35	3.5	2.3
<i>Interlinks</i>	Thickness (ti) [mm]	Number [-]	Wall thickness (t) [mm]	
Minimum	1	9	0.8	
Maximum	2.5	49	2.3	
<i>Bamboo nodes</i>	Radius (Rn) [mm]	Number [-]	Wall thickness [mm]	
Minimum	1	3	0.8	
Maximum	2	6	2.3	

from compression tests, described in the A.1 Appendix, with Young's modulus set to 227 MPa and Poisson's ratio at 0.43. The static Riks procedure is chosen to handle potential non-linearities, with boundary conditions set such that the lower plate is encastered and the upper plate constrained to move vertically, applying an initial displacement of 1 mm. The static Riks method used in this study addresses nonlinear static problems involving phenomena like buckling or collapse, capturing large displacements and nonlinear behavior beyond yielding. It is particularly suited for cases with unstable load-displacement curves, such as buckling, which linear static analysis cannot model. This method uses an arc-length continuation approach, incrementally solving for loads and displacements, ensuring stable tracking even during large deformations or loss of stability. The arc-length technique adjusts load increments based on the structure's behavior, preventing failure at critical points like buckling. Quadratic elements are used to represent the complex geometry and deformation of bio-inspired structures accurately. Convergence analyses for mesh sizes from 1 mm to 3 mm are conducted, ensuring that the maximum deviation in curvature control remains under 0.1 for accuracy. The detailed results from these analyses, presented in [Appendix A.2](#), demonstrate the approach implemented to validate the mechanical performance of the bio-inspired structures.

2.5. Multi-objective optimization

Given the multi-faceted morpho-structural characteristics of the designed architected structures, multi-objective optimization is pivotal for implementing bio-inspired structures that achieve optimal performance while meeting diverse criteria.

The optimization process is concentrated on minimizing the volume while maximizing the reaction force (objective functions). It focuses on bending loads due to the biomechanical relevance of flexural stresses in bio-inspired structures, particularly those modeled after natural forms like *Bamboo Nodes* and *Horsetail* plants. These structures are inherently optimized for environments dominated by lateral forces, where bending performance is critical. The four-point bending test is used to quantify the Reaction Force (RF), a key indicator of load-bearing capacity under flexural stress. This approach is aligned with the design's morpho-structural characteristics, which are intended to balance strength and flexibility. Given the trade-offs involved, optimizing for bending enables a focused exploration of structural efficiency, ensuring that the designs maintain high load-bearing capacity under bending while minimizing material usage, which is particularly suited to applications involving flexible, lightweight architectures.

The optimization process focuses on the *Horsetail*, *Interlinks*, and *Bamboo Nodes* designs, which are chosen for the interest in their practical applicability, and the *Intermediate* structure. The *Complete* feature is not considered because multi-feature structures inherently involve a higher number of variables and, consequently, a higher number of samples to ensure robust and reliable results. Instead, the behavior of this structure has been analyzed numerically, as detailed later.

The process focuses on defining a set of geometrical variables (eventually a combination of them) specific to each bio-inspired design

feature (as reported in detail in Table 1), such as those derived from horsetail plants, bamboo nodes, or interlink structures (Fig. 1B). These variables influence both the volume of the structure and its RF in the four-point bending test. The optimization's core challenge is navigating the trade-offs between minimizing the structural volume and maximizing the RF or achieving other specific goals, such as setting a desired volume while optimizing the RF. This necessitates a multi-objective optimization approach that balances these competing criteria. To tackle this, the optimization process incorporates both objective functions: 1) minimize the structures' volume and 2) maximize the RF.

Given its dependency on complex geometric parameters, the RF cannot be derived straightforwardly through algebraic equations. Instead, a regression model is used to predict it based on the geometric variables of Table 1. This model is developed using data from FEA conducted in ABAQUS/CAE, which simulate the performance of the structures under bending stress. Given the intricate nature of the bio-inspired designs and the testing setups, a regression approach allows for capturing the relationship between design parameters and performance metrics in an analytical form.

To generate the necessary data for the regression model, Sobol' sequences are utilized (Morgan and Kucherenko, 2020; Renardy et al., 2021). These sequences, known for their low-discrepancy properties, offer a quasi-random distribution of sample points that improve the accuracy of the regression model while minimizing the number of required simulations. Sobol' sequences ensure that the generated samples are uniformly distributed across the design space, which enhances the reliability of the resulting regression model. This approach is particularly valuable when dealing with complex designs where traditional random sampling might not provide sufficient coverage of the design space.

With the regression model in place, the optimization process exploits MATLAB2022 genetic algorithm solver, specifically the *gamultiobj* function. Genetic algorithms are well-suited for multi-objective optimization as they simulate the process of natural evolution through selection, crossover, and mutation. The algorithm starts with an initial population of potential solutions. It iteratively evolves this population by selecting the best-performing individuals (elite children), combining their features (crossover), and introducing random variations (mutation). This evolutionary process continues until an optimal set of solutions is identified.

The result of the genetic algorithm is the Pareto frontier, a collection of optimal solutions that represent different trade-offs between the objective functions. Each point on this frontier signifies a design where any improvement in one objective (e.g., increasing the RF) would compromise the other (e.g., increasing the volume). The Pareto frontier (here limited to a Pareto set of 50 values over a population of 100 individuals) provides a practical set of design options that balance volume and RF objective functions, enabling one to choose the most suitable design based on specific project requirements or constraints.

2.5.1. Optimization parameters

2.5.1.1. Sobol' sequence geometrical constraints. The number of samples used in the optimization process is different for each bio-inspired feature: the population of every sequence is increased until acceptable R-square (R^2) and Root mean square error (RMSE) values of the Reaction Force (RF) regression model are obtained. Some geometrical constraints, more precisely boundary conditions, are used in generating the Sobol' sequence, which is reported in Table 2. Since the *Intermediate* structure (Fig. 1C, left) is multi-featured, its Sobol' sequence constrained to the same range as the individual bio-inspired features.

After having numerically tested under four-point bending all the structures given as the Sobol' sequence output, the RF model regression is generated to find the analytical function describing the dependency of the RF on the bio-inspired features design parameters. To do that, a non-

linear regression model function is used, i.e., making a trade-off between accuracy and computational time. The function *fitnlm* was used to fit the polynomial model to the input values. To understand the result appropriateness, this function provides the R-square (R^2) and root mean square error (RMSE) in addition to the estimated coefficients for the fitting model. The regression model equations are reported in Eqs. (1)–(4). They describe the Reaction Force of *Horsetail*, *Interlinks*, *Bamboo Nodes* structures, and *Intermediate* structure, respectively, as a function of the geometrical parameters described in Table 2.

$$\begin{aligned} \text{RFHorsetail} = & b_0 + b_1x_1 + b_2x_2 + b_3x_3 + b_4x_4 + b_5x_1^2 + b_6x_2^2 + b_7x_3^2 \\ & + b_8x_4^2 + b_9x_1x_2 + b_{10}x_1x_3 + b_{11}x_1x_4 + b_{12}x_2x_3 + b_{13}x_2x_4 + b_{14}x_3x_4 \end{aligned} \quad \text{Eq. 1}$$

$$\begin{aligned} \text{RFInterlinks} = & b_0 + b_1x_1 + b_2x_2 + b_3x_3 + b_4x_1^2 + b_5x_2^2 + b_6x_3^2 + b_7x_1x_2 \\ & + b_8x_1x_3 + b_9x_2x_3 \end{aligned} \quad \text{Eq. 2}$$

$$\begin{aligned} \text{RFBambooNodes} = & b_0 + b_1x_1 + b_2x_2 + b_3x_3 + b_4x_1^2 + b_5x_2^2 + b_6x_3^2 \\ & + b_7x_1x_2 + b_8x_1x_3 + b_9x_2x_3 \end{aligned} \quad \text{Eq. 3}$$

$$\begin{aligned} \text{RFIntermediate} = & b_0 + b_1x_1 + b_2x_2 + b_3x_3 + b_4x_4 + b_5x_5 + b_6x_6 + b_7x_1^2 \\ & + b_8x_2^2 + b_9x_3^2 + b_{10}x_4^2 + b_{11}x_5^2 + b_{12}x_6^2 + b_{13}x_1x_2 + b_{14}x_1x_3 + b_{15}x_1x_4 \\ & + b_{16}x_1x_5 + b_{17}x_1x_6 + b_{18}x_2x_3 + b_{19}x_2x_4 + b_{20}x_2x_5 + b_{21}x_2x_6 + b_{22}x_3x_4 \\ & + b_{23}x_3x_5 + b_{24}x_3x_6 + b_{25}x_4x_5 + b_{26}x_4x_6 + b_{27}x_5x_6 \end{aligned} \quad \text{Eq. 4}$$

Once the objective function formulation is obtained, the multi-objective optimization can be implemented, exploiting the *Optimization* toolbox, which allows the user to set different options for the optimization problem resolution. For each variable, the lower and the upper bounds are defined (Table 2), and for the variables representing feature numbers Table 2, an integer constraint was added. The solver *gamultiobj* – *Multiobjective optimization* is selected using the genetic algorithm; the optimization output is the so-called Pareto frontier.

3. Results and discussion

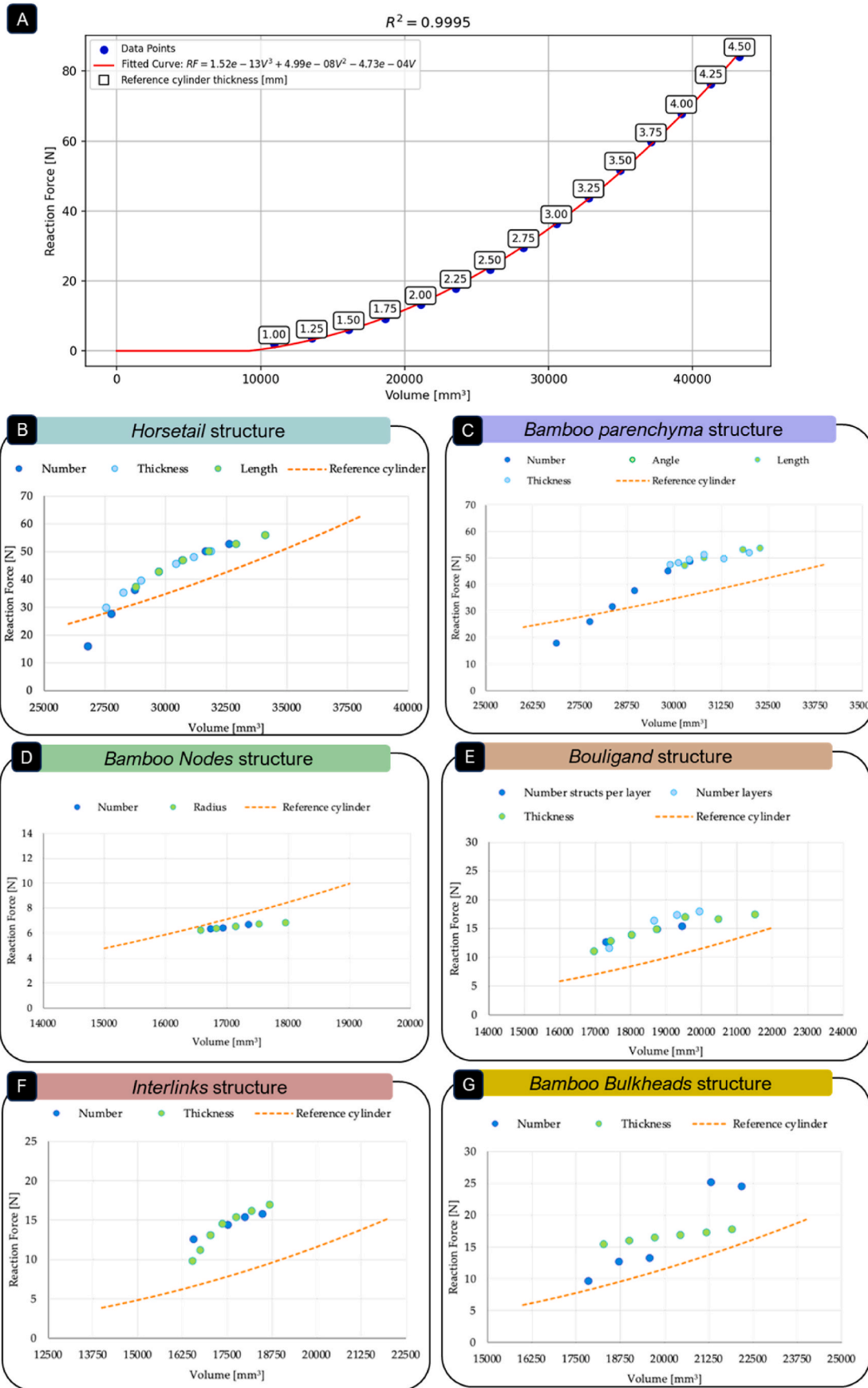
This study aims to understand the role of features found in promising natural structures, particularly their morpho-structural characteristics, to optimize hollow cylinders for multiple loading actions, including bending and compression. A multi-objective parametric optimization is implemented to achieve structures that maximize bending resistance while minimizing volume, yielding optimal Pareto solutions, and showing significant resistance improvements compared to hollow cylinders of equivalent volume. The improvement of bio-inspired optimized solutions is proven via a combination of numerical and experimental strategies, which also allow for assessing the practical feasibility of the designed structures. All the results obtained are presented and discussed below.

3.1. Bending-resistant bio-inspired architected structures

3.1.1. Bio-inspired feature selection based on numerical results

Fig. 2A shows the reaction force versus volume bending trendline of the 15 reference hollow cylinders to aid the comparison between bio-inspired structures and the reference of the same volume. The nonlinearity observed in the RF-V relationship is attributed to variations in wall thickness, with thinner walls exhibiting more significant deformations and ovalization phenomena than thicker ones.

The *Horsetail* performance is evaluated regarding rib number, thickness, and length, whose values range in accordance with Table 1. Fig. 2B indicates that increasing rib number enhances RF, peaking around 25 ribs. Thicker ribs consistently improve RF, with a plateau at



(caption on next page)

Fig. 2. Bio-inspired features selection based on bending numerical performances. The designed bio-inspired structures and the hollow cylinder are analyzed through Finite Element Analysis to observe the influence of the feature parameters on the output Reaction Force, obtained by imposing 1 mm of vertical displacement to the loading pins. **A.** Variation of Reaction Force (RF) values as a function of the hollow cylinder Volume (V) described by a quadratic fit ($R^2 = 0.99$) of equation $RF = aV^3 + bV^2 + cV$ with $a = 1.52e-13$, $b = 4.99e-08$, $c = -4.73e-04$. The framed numbers indicate the wall thicknesses of the hollow cylinders. **B.** RF-V relationship in the *Horsetail* structure, as a function of the number (Zappa et al., 2024; Wang and Li, 2020; Buccino et al., 2021a; Khoshgoftar et al., 2022; Mirzaali et al., 2017; Libonati et al., 2020; Bru et al., 2020; Wegst and Ashby, 2004; Mirzaali et al., 2018; Libonati and Vergani, 2014; Buccino et al., 2022b; Qu et al., 2024; Zhou et al., 2024; Shi et al., 2024; Xiong et al., 2023; Rohde et al., 2018; Niknam and Akbarzadeh, 2020; du Plessis et al., 2019; Maconachie et al., 2019; Mirzaali et al., 2020; Tran et al., 2017; Mueller et al., 2018; Ha et al., 2024; Ha et al., 2023; Saldívar et al., 2023; Yaraghi et al., 2016; Saldívar et al., 2022; Mistry et al., 2023; Powelson and Yang, 2011; Tavangarian et al., 2019; Gao et al., 2016), thickness [0.4–1.6 mm], and length [1–3.5 mm] of the bio-inspired features with respect to the reference cylinder. **C.** RF-V relationship in the *Bamboo Parenchyma* structure, as a function of the number (Zappa et al., 2024; Wang and Li, 2020; Buccino et al., 2021a, 2022b; Khoshgoftar et al., 2022; Mirzaali et al., 2017, 2018; Libonati et al., 2020; Bru et al., 2020; Wegst and Ashby, 2004; Libonati and Vergani, 2014; Qu et al., 2024; Zhou et al., 2024; Shi et al., 2024; Xiong et al., 2023; Rohde et al., 2018), angle [30–55°], length [1.5–2.5 mm], and thickness [0.2–0.6 mm] of the bio-inspired features with respect to the reference cylinder. **D.** RF-V relationship in the *Bamboo Nodes* structure, as a function of the number (Sullivan et al., 2017; Buccino et al., 2022a; Zappa et al., 2024; Wang and Li, 2020) and radius [1–2 mm] of the bio-inspired features with respect to the reference cylinder. **E.** RF-V relationship in the *Bouligand* structure, as a function of the number of struts per layer (Sullivan et al., 2017; Buccino et al., 2021a, 2022a; Zappa et al., 2024; Wang and Li, 2020; Khoshgoftar et al., 2022; Mirzaali et al., 2017), number of layers (Wang and Li, 2020; Buccino et al., 2021a, 2022b; Khoshgoftar et al., 2022; Mirzaali et al., 2017, 2018; Libonati et al., 2020; Bru et al., 2020; Wegst and Ashby, 2004; Libonati and Vergani, 2014; Qu et al., 2024; Zhou et al., 2024; Shi et al., 2024), and thickness [1.0–2.5 mm] of the bio-inspired features with respect to the reference cylinder. **F.** RF-V relationship in the *Interlinks* structure, as a function of the number (Mirzaali et al., 2017; Libonati et al., 2020; Bru et al., 2020; Wegst and Ashby, 2004; Mirzaali et al., 2018; Libonati and Vergani, 2014; Buccino et al., 2022b; Qu et al., 2024; Zhou et al., 2024; Shi et al., 2024; Xiong et al., 2023; Rohde et al., 2018; Niknam and Akbarzadeh, 2020; du Plessis et al., 2019; Maconachie et al., 2019; Mirzaali et al., 2020; Tran et al., 2017; Mueller et al., 2018; Ha et al., 2024; Ha et al., 2023; Saldívar et al., 2023; Yaraghi et al., 2016; Saldívar et al., 2022; Mistry et al., 2023; Powelson and Yang, 2011; Tavangarian et al., 2019; Gao et al., 2016; Chen et al., 2017; Buccino et al., 2022c; Li et al., 2022; Lindberg et al., 2018; De Vivo Nicoloso et al., 2021; Fayemi et al., 2017; Katiyar et al., 2021; Buccino et al., 2021b; Chen et al., 2018; Osorio et al., 2018; Amada et al., 1997; Umer et al., 2014; Wegst, 2011; Svatik et al., 2021) and thickness [1.0–2.5 mm] of the bio-inspired features with respect to the reference cylinder. **G.** RF-V relationship in the *Bamboo Bulkheads* structure, as a function of the number (Yin et al., 2019; Sullivan et al., 2017; Buccino et al., 2021a, 2022a; Zappa et al., 2024; Wang and Li, 2020) and thickness [0.75–2.0 mm] of the bio-inspired features with respect to the reference cylinder.

higher thicknesses and an optimal rib length between 1.5 mm and 2 mm. The *Horsetail* structure significantly outperforms the reference cylinder in RF. The *Bamboo Parenchyma* showed a rise in RF with more reinforcements, peaking at 17 ribs, as depicted in Fig. 2C. Thicker reinforcements also improve RF, while longer reinforcements maintain stable percentage differences; variations in angle have a minor effect on RF. This structure demonstrates substantial RF improvements compared to the reference cylinder. For the *Bamboo Nodes* structure, Fig. 2D shows that increasing the number and radius of reinforcements enhances RF. However, the percentage differences are less pronounced compared to other bio-inspired structures. Some configurations approach the RF values of reference cylinders, suggesting potential for further optimization. The *Bouligand* performance, shown in Fig. 2E, improves with increased reinforcements per layer and thickness, with optimal performance around 1.25 mm. While the number of ribs per layer has a lower influence, the *Bouligand* structure achieves significant RF improvements over reference cylinders. In the *Interlinks* structure, Fig. 2F reveals that increasing the number and thickness of reinforcements leads to substantial RF enhancements. The optimal thickness is around 1.75 mm, and increasing reinforcement number consistently improves RF, with percentage differences exceeding 80%. Tests with thicker walls confirm higher RF values for bio-inspired structures, though with smaller percentage differences. The *Bamboo Bulkheads* configuration, illustrated in Fig. 2G, shows improved RF with more bulkheads, peaking at 3 and 6 due to their proximity to the loading pins. The thickness of bulkheads also plays a significant role in RF improvement. All configurations appear promising, with the number of bulkheads likely being the most influential parameter.

Bio-inspired structures generally outperform reference hollow cylinders in RF for the same volume due to optimized inertia moments and bending load conditions. Combining features may yield even better performance, with multi-featured designs balancing the ease of 3D printing and effectiveness. Fig. 2B–G highlights how bio-inspired features impact RF improvements, emphasizing the dependency of feature performance on base geometry and the need for morpho-structural optimization.

3.1.2. Architected structure optimization

The optimization, at bending, of the bio-inspired structural designs yields key results, particularly for single-feature structures (Fig. 3A–C).

The *Horsetail* structure, with its rib configurations, exhibits superior strength and performance (Fig. 2B), confirming its selection for further evaluation. If compared to a commercially available double-layer axially hollow pipe, this bio-inspired approach— analogously considered in the *Bamboo Parenchyma*—leverages Nature’s design principles and, with advanced additive manufacturing, enables versatile exploration of rib configurations and future consideration of multi-material solutions for enhanced performance. Similarly, the *Interlinks* and *Bamboo Nodes* structures are chosen for their distinct reinforcement strategies, showing variable effectiveness depending on the application. Due to the increased complexity of multi-feature designs, only the *Intermediate* structure (Fig. 1C, left) is analyzed (Fig. 3D). Using the Sobol’ sequence for sampling is crucial, as this quasi-random sequence method ensures a uniform distribution of samples across the variable space, thereby providing a comprehensive representation of the design space.

The sample sizes are tailored to the complexity of each structure (Fig. 3E), opting out for a tradeoff choice between the goal of capturing optimization trends and fitting the data. For the *Horsetail*, a total of 50 samples were utilized, which is sufficient given its relatively simple design with fewer variables. In contrast, the *Bamboo Nodes* and *Interlinks* structures require 20 and 35 samples, respectively, due to their slightly more complex configurations. For the *Intermediate* structure (Fig. 1C, left), a larger sample set of 70 is used to account for its multi-faceted (while complex) design, allowing for a thorough exploration of each design’s performance characteristics.

FEA results of the optimized structures provide a detailed comparison of the RF versus V for the different bio-inspired structures. Fig. 3A shows that the *Horsetail* configurations generally outperformed the reference cylinder in RF, with specific configurations achieving notable improvements. This suggests that the *Horsetail* design, with its unique rib configurations, enhances structural performance effectively. In contrast, the *Bamboo Nodes*, as illustrated in Fig. 3C, exhibited lower RF values relative to the reference cylinder at similar volumes, indicating that this design may not offer significant advantages in terms of structural strength. The *Interlinks* structure performance, depicted in Fig. 3B, consistently surpassed the reference cylinder in RF across various configurations. This superior performance is attributed to its internal reinforcement strategies, which enhance bending resistance. The *Intermediate* structure, shown in Fig. 3D, displays promising results with improved RF values at various volumes, demonstrating the benefits of

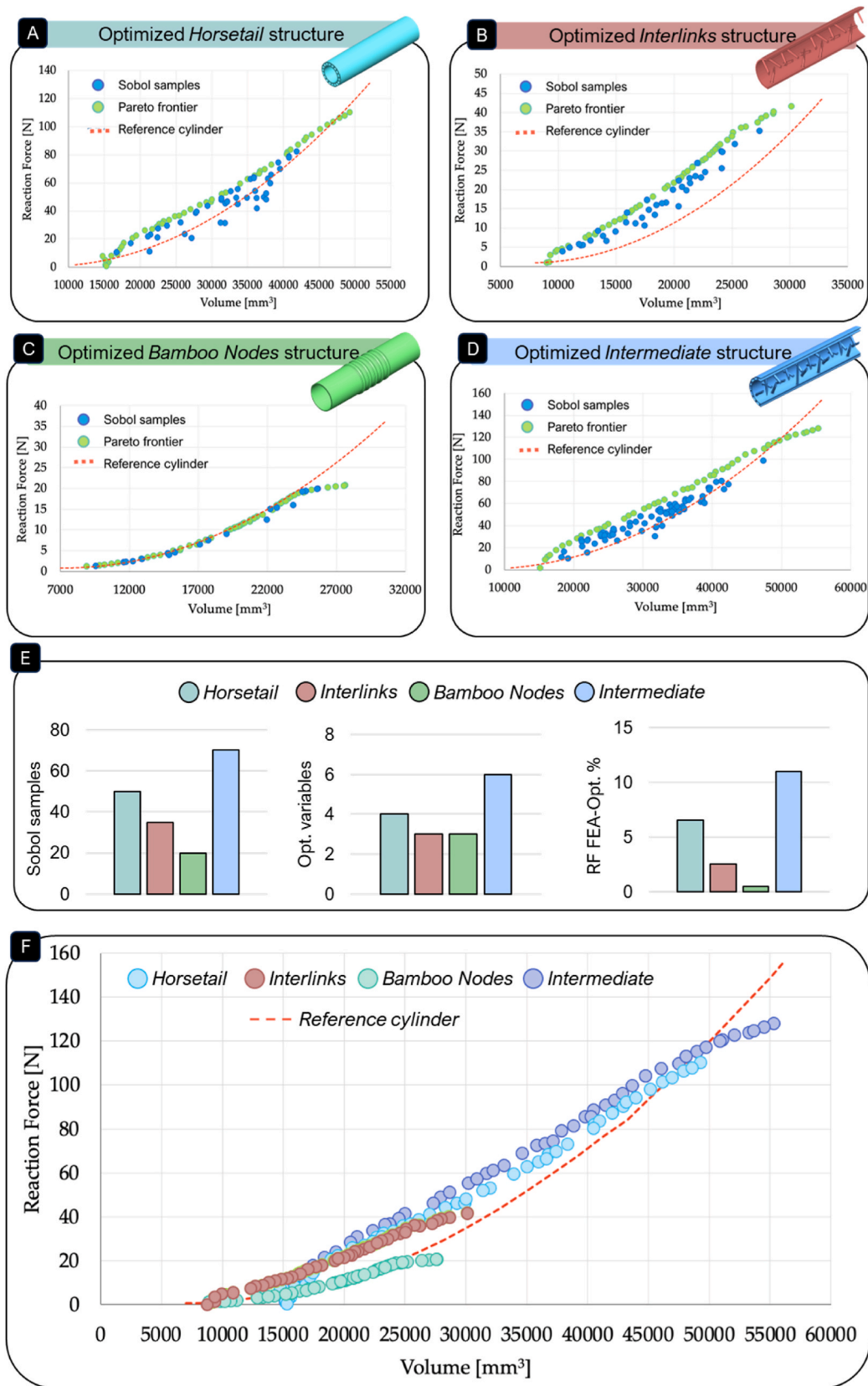


Fig. 3. Architected structure optimization **A.** RF-V relationship for the *Horsetail* structure, Sobol sequence, and Pareto set with respect to the reference cylinder. **B.** RF-V relationship for the *Interlinks* structure, Sobol sequence, and Pareto set with respect to the reference cylinder. **C.** RF-V relationship for the *Bamboo Nodes* structure, Sobol sequence, and Pareto set with respect to the reference cylinder. **D.** RF-V relationship for the *Intermediate* structure, Sobol sequence, and Pareto set with respect to the reference cylinder. **E.** Validation of the optimization process: number of Sobol samples, optimization variables (see Table 2), and reaction force of the initial vs. optimized structure obtained through finite element analysis (reported as % difference). **F.** Comparison of the Pareto sets of the four considered architected structures.

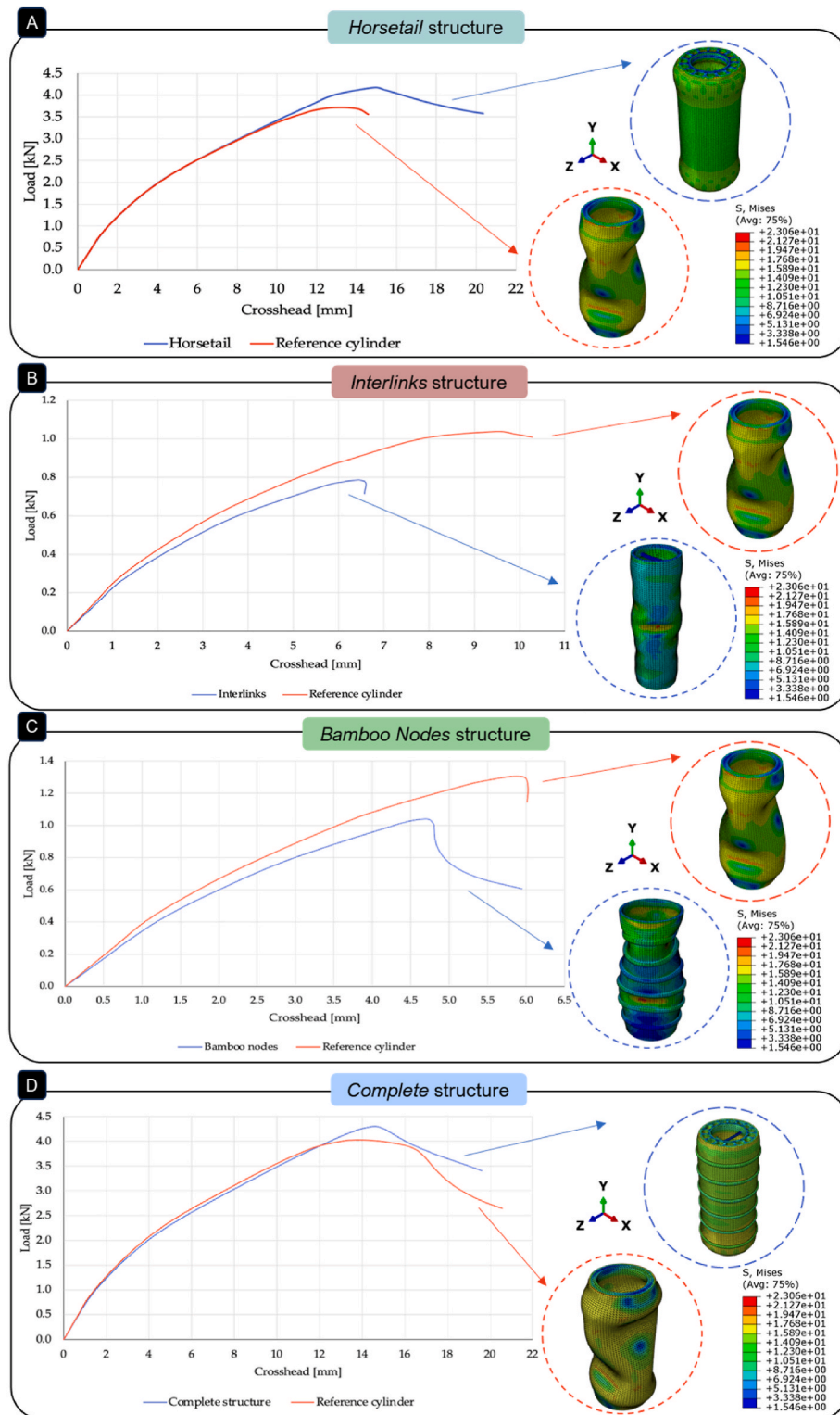


Fig. 4. Compression-resistant bioinspired architected structure numerical analyses compared to the relative reference cylinder. The results are plotted as a function of the load and crosshead displacement. On the right the deformed shape is reported, together with the von Mises stresses. A. *Horsetail* structure numerical results. B. *Interlinks* structure numerical results. C. *Bamboo Nodes* structure numerical results. D. *Complete* structure numerical results.

combining features from single-feature designs.

The regression models developed for each structure, as summarized in paragraph 2.5.1, show high R^2 values, indicating the model's accuracy in predicting RF based on design parameters (Fig. 2). The Pareto frontier analysis, which evaluates the trade-offs between RF and V, further elucidates the design efficiency of each structure. For the

Horsetail structure, the Pareto front (Fig. 3F) indicates that configurations with smaller volumes generally had lower RF compared to the reference cylinder, revealing that configurations with increased rib thickness and number tend to achieve better RF performance. Similarly, the *Interlinks* Pareto front shows that maximizing the thickness of reinforcing struts while minimizing their number results in superior RF

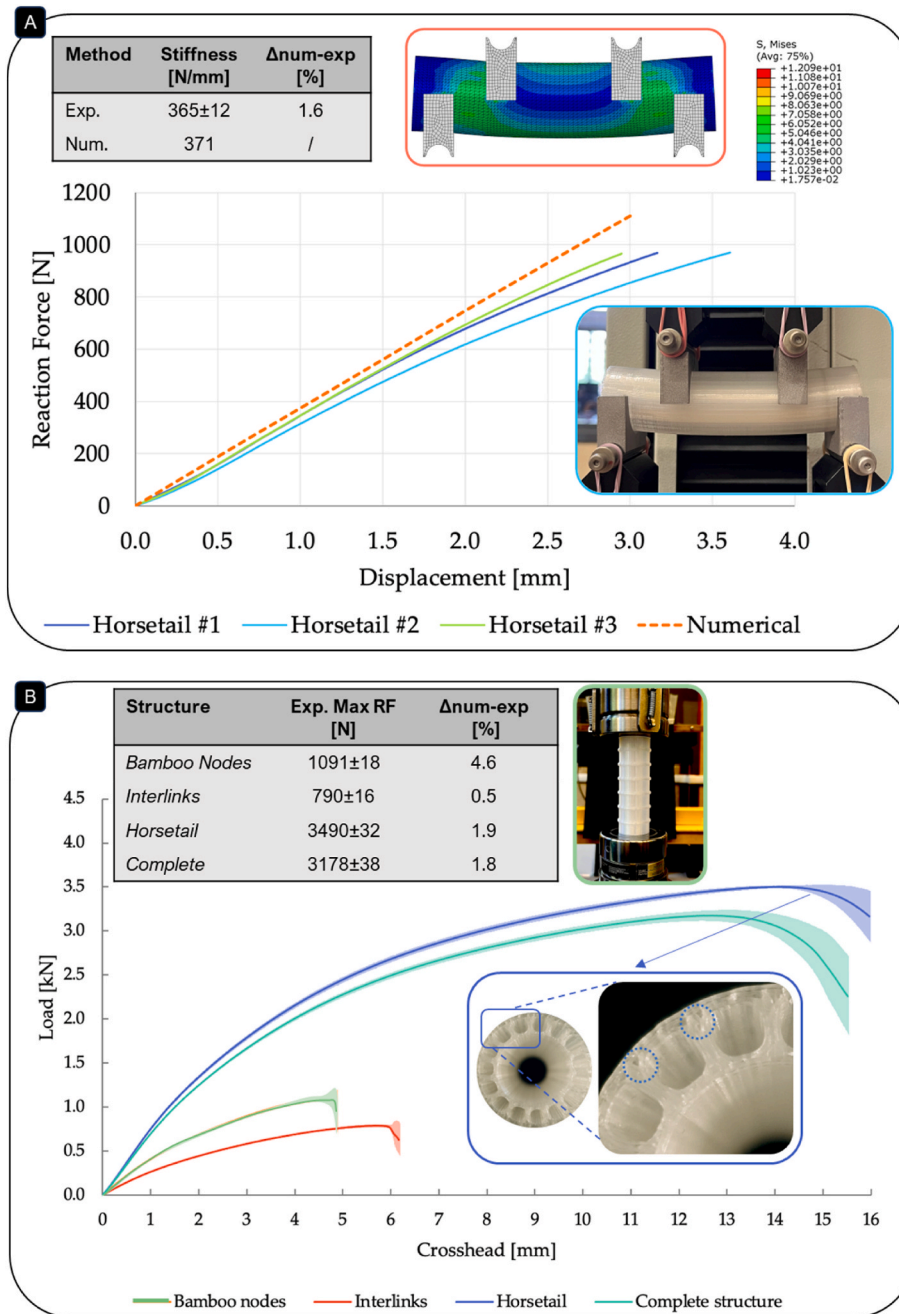


Fig. 5. Experimental validation of the numerical analyses for both the bending- and the compression-resistant bio-inspired structures. **A.** Experimental and numerical four-point bending test results comparison for the *Horsetail* structure. Numerical and experimental stiffness are reported, together with their percentage difference in the table (gray box). A schematic of the improved numerical simulation (including the supports) in accordance with the experimental setup is sketched. **B.** Overview of the bio-inspired structures under experimental compression tests (an example of the setup is reported for the *Bamboo Nodes* structure). The percentage difference of the numerical and experimental results for each structure is reported in the table (gray box). Local printing defects, highlighted specifically for the *Horsetail* structure, and inducing the 1.9% discrepancy in experimental results, are shown.

performance; in contrast, the *Bamboo Nodes* Pareto front reveals that this design does not offer substantial advantages over the reference cylinder, with optimal configurations often lying on or below the reference curve. The *Intermediate* structure’s Pareto front combines features from both the *Interlinks* and *Horsetail* structures, demonstrating improved RF performance at larger volumes by leveraging the strengths of its constituent designs.

Validation of the optimization process shows that the predicted and actual RF values and volumes align closely, though some discrepancies, particularly for the *Intermediate* structure, highlighting areas for potential improvement. Increasing the sample size for the Sobol’ sequence

could enhance model accuracy and reduce these discrepancies. Despite the challenges in manufacturing certain bio-inspired features, the *Intermediate* structure stands out as the most promising design, effectively combining features to achieve superior performance compared to single-feature structures.

Herein, genetic algorithms effectively optimize bio-inspired structures by balancing structural volume and reaction force under bending stress. While the genetic algorithm generates a Pareto frontier of optimal solutions, it does not directly provide explicit mathematical relationships between design variables and objectives. Regression models, detailed in Eqs. (1)–(4), approximate these relationships, linking

geometric parameters (Table 2) to RF and volume. A third-order polynomial regression effectively captures these connections, while advanced methods like kriging may be needed for more complex cases. Sobol' sequences enhance regression accuracy with fewer simulations, serving as surrogates for FEA simulations and guiding the refinement of bio-inspired designs.

3.2. Compression-resistant bio-inspired architected structures

To advance structural integrity through bio-inspired engineering, numerical compression tests are conducted on various structural models, including the *Horsetail*, *Bamboo Nodes*, *Interlinks*, and *Complete* structures. For the first three structures, simulations are performed with optimized bio-inspired features. The *Horsetail*-inspired structure (Fig. 4A) significantly improves compressive strength, attaining an RF 12.41% greater than the reference hollow cylinder and demonstrating a displacement before buckling 10.52% higher. This enhancement is attributed to the bio-inspired cross-sectional geometry, which effectively mitigates buckling instability by incorporating an array of reinforcing ribs and an inner cylindrical wall. Conversely, the *Interlinks* and *Bamboo Nodes* structures do not achieve comparable performance gains. The *Interlinks* structure (Fig. 4B) exhibits localized buckling, manifesting as outward and inward bulges, compromising its structural integrity under compression. Similarly, the *Bamboo Nodes* suffer from substantial deformation due to insufficient internal support, although external ridges partially mitigate bulging (Fig. 4C). The *Complete* structure, which integrates features from all three bio-inspired designs, shows an improvement over the reference cylinder, with an RF 6.73% higher and a displacement 5.61% greater before buckling (Fig. 4D). However, this composite structure performance does not exceed that of the *Horsetail*-inspired design alone, suggesting that the additional components do not contribute significant advantages. The findings, as detailed in Fig. 4, highlight the superior efficacy of the *Horsetail*-inspired design in enhancing compressive performance and stability while also underscoring the limitations of the *Interlinks* and *Bamboo Nodes* configurations.

3.3. Architected structure experimental validation

As per the transposition to technology, the four-point bending test has been employed to validate the numerical simulations and the entire optimization process for the *Horsetail* structure. The experimental data shown in Fig. 5A reveals high congruence with the numerical simulations. A comparative analysis of the experimental and numerical results is conducted by examining the slope of the load-displacement curves within the range of 0.5 mm–1 mm (results are reported in Fig. 5A in the table): the minimal percentage differences observed confirm the successful validation of the numerical model, thereby endorsing the accuracy of the four-point bending simulations utilized throughout this study. The methodological distinction between the optimization phase and the validation phase is notably marked by the transition from cylindrical pins to custom supports for load application, as illustrated in Fig. 5A. Indeed, incorporating custom supports and encastre boundary conditions allows to more accurately reflect experimental setups and mitigate issues such as slippage and incision. This demonstrates that customized supports (Fig. 5A) effectively constrained the structure, enhancing its load-bearing capacity.

In the compression experimental tests (see Fig. 5B), all the experimental data exhibited a strong alignment with numerical predictions, evidenced by minimal percentage differences in maximum load and displacement, as outlined in the gray box of Fig. 5B. However, the results

indicated that the *Bamboo Nodes* feature do not significantly improve the buckling resistance of the hollow cylinder. Variations in buckling modes are attributed to manufacturing imperfections and non-central loading. Further analysis of the *Interlinks* structure corroborated the numerical findings, affirming the accuracy of the simulations, although some minor discrepancies are noted in displacement measurements. For the *Horsetail* structure, experimental results in Fig. 5B demonstrate substantial improvements in buckling resistance compared to reference hollow cylinders. The *Horsetail* structure significantly increases both displacement before buckling and maximum load, indicating superior performance. Eventually, local defects in the manufacturing process (as highlighted in Fig. 5B) may induce alterations in the maximum reaction force, with increased variability in the sample pool. The numerical results generally align with experimental trends, though deviations in the final stages of loading are observed. Differences in deformation patterns may be attributed to manual positioning errors during testing: to address them, simulations incorporating varying degrees of eccentricity are conducted, revealing that increasing eccentricity leads to deformed shapes more closely aligned with experimental observations (applying 0.1 mm eccentricity in the numerical simulation leads to 89% increase in the match with the experimental values). In the next stage, studies should consider incorporating geometric porosities and adopting orthotropic material models to better represent the anisotropic nature of the manufactured specimens. Finally, compression tests of the *Complete* structure versus the reference cylinder indicate comparable maximum forces but superior displacement capabilities for the *Complete* structure. This suggests that while the *Complete* configuration does not surpass the reference cylinder in maximum force, it exhibits enhanced displacement characteristics (+24%) before buckling.

As a general remark, each bio-inspired structure is experimentally and numerically paired with its reference cylinder, allowing for a focused comparison between the bending and compression responses of the bio-inspired designs. The curves related to bending and compression of the reference cylinders show a good agreement with the corresponding numerical results, with deviations of less than 5%, confirming the accuracy and reliability of the numerical model. Herein, the study prioritizes evaluating the relative performance of the bio-inspired structures, which demonstrate a significant improvement in compressive strength and stability compared to their respective reference cylinders.

3.4. Overall efficacy of the morpho-structural optimization on the mechanical response

Overall, in evaluating the bending behavior of the optimized bio-inspired architected structures, the data presented in Fig. 3F illustrates that, while the *Bamboo Nodes* structure does not show any improvement over the reference hollow cylinders despite optimization, both the *Interlinks* and *Horsetail* exhibited significant enhancements. Specifically, both structures demonstrated approximately a 100% increase in RF under optimal conditions, i.e., for reduced volumes. However, the percentage improvement decreases for higher volume configurations within the *Interlinks* set, suggesting diminishing returns. Consequently, the *Horsetail* structure is recommended to delay the occurrence of instability phenomena (maximum displacement reached +40% with respect to the reference cylinder). Additionally, the *Intermediate* structure, which integrates *Horsetail* ribs and *Interlinks*, achieves up to 20% higher reaction forces than its reference counterpart while maintaining the same volume. It is noteworthy that at larger volumes (greater than 47,000 mm³), the effectiveness of reinforcements wanes due to the excessive wall thickness of the reference cylinder. Despite this, the bio-

inspired configurations have demonstrated the capability to nearly double the reaction force compared to the reference cylinders (Fig. 5A), validating the effectiveness of combining bio-inspired design principles with parametric multi-objective optimization.

Regarding compressive performance, as depicted in Fig. 5B, the *Bamboo Nodes* and *Interlinks* structures prove ineffective in enhancing compression resistance or delaying buckling compared to their reference cylinders, with reductions in maximum reaction force of up to 20%. The analysis highlights that increasing volume in these features negatively impacts resistance, primarily because the cylindrical wall's load-bearing capacity is compromised. Conversely, the *Horsetail* structure exhibited superior compressive performance, surpassing its reference cylinder by approximately 20% in reaction force and demonstrating enhanced resistance to buckling. The *Complete* structure also shows improved performance, with a maximum reaction force 1% higher and displacement over 20% greater than the reference cylinder, attributable primarily to the optimized *Horsetail* ribs. Thus, the *Horsetail* is the preferred choice for compressive loading due to its superior resistance and ease of manufacturing.

In conclusion, bio-inspiration emerges as a leading paradigm in bio-inspired structure design, driven by advancements in contemporary manufacturing technologies. By emulating the hierarchical architectures and evolutionary refinements found in Nature, it becomes possible to transform materials with ordinary mechanical properties into structures that exhibit remarkable resistance to various types of loads. Here, the geometric parameters inherent to bio-inspired features covering plants and natural reinforcements are systematically optimized to address specific loading conditions, geometric constraints, and project requirements. A multi-objective parametric optimization approach has proven essential to identify optimal Pareto solutions, yielding custom-designed structures that balance maximum bending resistance with minimal volume. Comparative analysis reveals that bio-inspired structures generally outperform equivalent-volume hollow cylinders in terms of resistance. The *Horsetail*-inspired structure demonstrates exceptional post-buckling performance, with superior maximum force and displacement metrics. The feasibility of these models is verified through experimental validation using structures fabricated via FFF techniques, confirming the reliability of the numerical models with acceptable percentage differences.

Despite the promising results, this study has some inherent limitations. The FFF printing has introduced some variability in the printed structures due to layer adhesion issues and minor defects. These imperfections can impact the mechanical performance of the samples. The study scope is also limited to specific bio-inspired features, potentially overlooking other natural designs that could offer further improvements. Also, the manual positioning of samples in testing apparatuses introduces potential misalignments, affecting the consistency of the loading conditions and resulting in variability in the experimental data.

Future research will pave the way for the multi-material design of architected bio-inspired structures. For instance, filling the interstitial spaces in the *Horsetail* structure (Fig. 1C) with a lower-density material enhances bending resistance with minimal weight increase, achievable with a multi-extruder FFF printer. Ensuring material adhesion is critical to prevent premature failure. Specifically, applying these optimized strategies to practical designs, such as in the biomechanical world (i.e., in transibial prostheses design), presents a promising avenue: these

structures require high strength and stiffness while maintaining low weight, making these additively manufactured bio-inspired structures ideal candidates. Future studies also could address fatigue behavior to ensure long-term durability in practical applications. Furthermore, expanding the optimization framework to include other loading conditions, such as torsion and impact, and integrating advanced manufacturing techniques like 3D printing with continuous fiber reinforcement could unlock new potential in bio-inspired structural design of optimized architected solutions.

4. Conclusion

This research successfully demonstrates the potential of bio-inspired, multi-scale design principles combined with multi-objective optimization to enhance structural performance while minimizing weight. By focusing on hollow cylinders, commonly used in engineering, the study addresses the challenge of maintaining stiffness and stability while reducing material. Among the evaluated architected structures, the *Horsetail* structure proved the most effective, showing a 100% increase in reaction force under bending, a 40% improvement in displacement before instability, and a 20% increase in compressive resistance compared to the reference cylinder. The experimental and numerical validation confirms the accuracy of these models, and the feasibility of fabricating such designs via 3D printing opens the door to practical applications, including the development of next-generation materials and structures that are both efficient and resilient.

CRedit authorship contribution statement

Alessia Senatore: Investigation, Data curation. **Mattia Venza:** Validation, Investigation, Data curation. **Sara Candidori:** Writing – review & editing, Methodology, Investigation, Data curation. **Serena Graziosi:** Writing – review & editing, Supervision, Resources, Methodology, Investigation. **Federica Buccino:** Writing – review & editing, Writing – original draft, Validation, Supervision, Resources, Methodology, Investigation, Data curation, Conceptualization.

Disclosure statement

The authors report there are no competing interests to declare.

Data availability

The data that support the findings of this study are available from the corresponding author upon reasonable request.

Declaration of competing interest

The authors declare that they have no known competing financial interests or personal relationships that could have appeared to influence the work reported in this paper.

Acknowledgements

The authors acknowledge Professor Laura Vergani for her methodological support in bio-inspired design.

Appendix A

A.1 Base material characterization

Base material tensile tests Relevant mechanical properties of Ultimaker Polypropylene (PP) are provided in Table A1.1.

Table A1.1
Mechanical properties of Ultimaker Polypropylene (PP).

Property	Value
Tensile modulus	220 MPa
Poisson ratio	0.43
Yield stress	8.7 MPa
Strain at yield	18%
Strain at break	>300%
Relative density	0.89

These values are obtained using a 0.4 mm nozzle, 90% infill, and XY plane printing. A tensile test following ASTM D638 is performed to verify these values under different printing parameters used in this work. Type IV specimens, shown in Fig.A1.1A, are chosen for efficiency. Three configurations are printed: Flat, On-edge, and Up-right, as shown in Fig.A1.1B. Printing parameters are listed in Table A1.2.

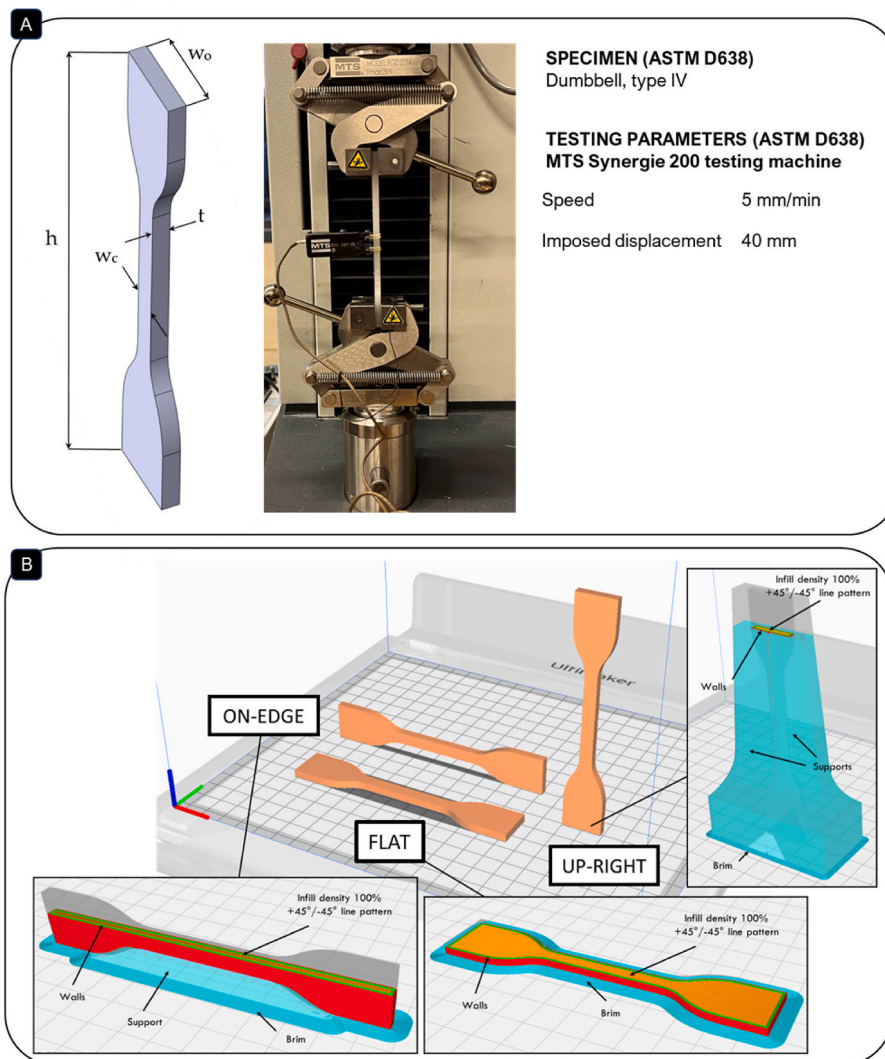


Fig. A1.1. Base material sample printing and testing under tensile loads. **A.** Testing setup and parameters. **B.** Specimen printing. Three directions are considered: on-edge, flat, and up-right.

Table A1.2
Printing parameters for characterization specimen.

Parameter	Specimen	Support PVA	Support PLA
Cura profile	Fine	Fine	Fine
Layer height	0.2 mm	0.2 mm	0.2 mm
Line width	0.38 mm	0.38 mm	0.35 mm
Infill density	100%	50%	20%
Build plate adhesion type	Brim	–	Brim
Brim width	5 mm	–	5 mm
Printing temperature	205 °C	215 °C	200 °C
Print speed	25 mm/s	35 mm/s	70 mm/s
Prime blob	Enabled	Enabled	Enabled

Supports are needed for up-right and on-edge configurations using PVA and PLA, respectively. The MTS Synergie 200 testing machine, with a maximum load capacity of 1 kN, is exploited for tensile tests. It records displacement, load, and time. Specimens are held with appropriate grips (Fig. A1.1A). Tests follow ASTM D638. An MTS 632.26F-20 axial extensometer (8 mm gauge length) is used for initial stress-strain data, removed after 1 mm displacement. The specimen's gauge length is 25 mm, with grips 65 mm apart. The upper grip moves at 5 mm/min to maintain quasi-static conditions. Calibration to zero load and displacement is performed before testing. Testing continues until 40 mm displacement.

Fig. A1.2 shows the tensile test results for the material characterization: the printing direction leads to different material curves.

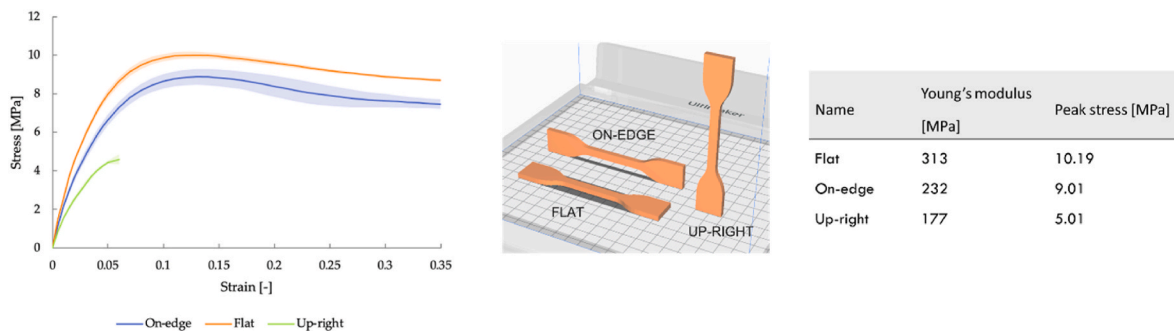


Fig. A1.2. Tensile test results on the base material. The average Young's modulus and peak stress are reported for each configuration. Three replicas are tested for each group.

The *Flat* and the *On-edge* configurations result in similar ductile behavior. The former configuration reaches higher stresses because the material layers are oriented parallel to the loading direction for a larger portion of the surface. Indeed, observing the specimens in the gauge region, the *Flat* adhesion area extends for about 6 mm (width), whereas for the *On-edge* one, it is only about 4 mm (thickness). The *Up-right* configuration shows brittle behavior and a minimal elongation compared to the others. Once again, imaging the 3D printed sample as a fiber-reinforced composite, the traction is applied normally to the fiber direction, testing the matrix, that is, the resistance of the layer adhesion.

Base material compression tests

Since the datasheet lacks compressive properties, a compression test following ASTM D695 [117] is conducted. The standard, typically for injection-molded plastics, is also applied to 3D-printed specimens [118], [119]. A prismatic, square-based specimen, shown in Fig.A1.3A, is used.

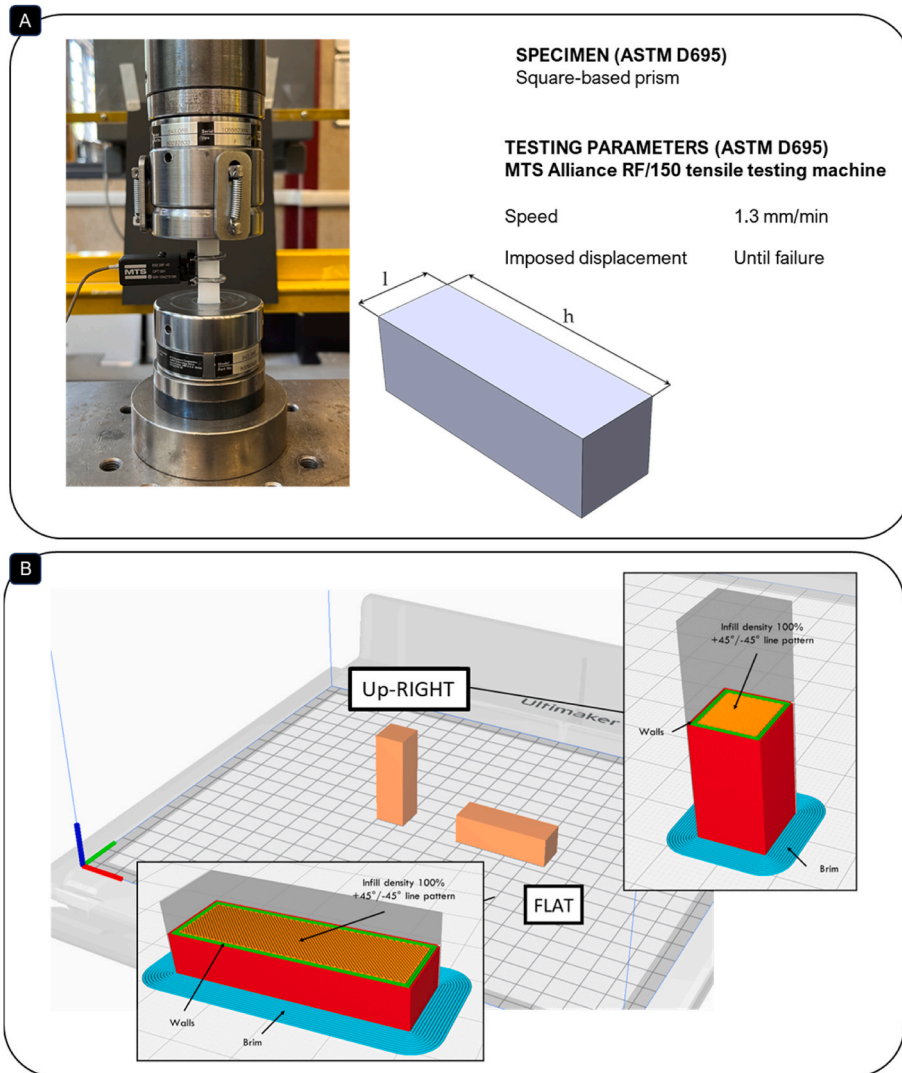


Fig. A1.3. Base material sample printing and testing under compressive loads. A. Testing setup and parameters. B. Specimen printing. Two directions are considered: flat, and up-right.

Two configurations, Flat and Up-right, differing in printing direction, are analyzed, as shown in Figure A1.3B.

Three samples are printed for each configuration.

The MTS Alliance RF/150 machine, capable of reaching 150 kN, is used for compression tests. It records displacement, load, and time and is equipped with compression plates (Fig.A1.3A). Tests followed ASTM D695. Samples are centered on the lower plate, and the upper plate is lowered until contact. An MTS 632.26F-40 axial extensometer (12 mm gauge length) records initial displacement up to 1 mm. Calibration to zero load and displacement is performed before testing. Samples are compressed at 1.3 mm/min until plastic instability, then unloaded.

Fig. A1.4 reports the results of the tests performed to characterize the material properties in compression. The different printing directions lead to different material responses, as highlighted in the tensile tests, which show an anisotropic behavior.

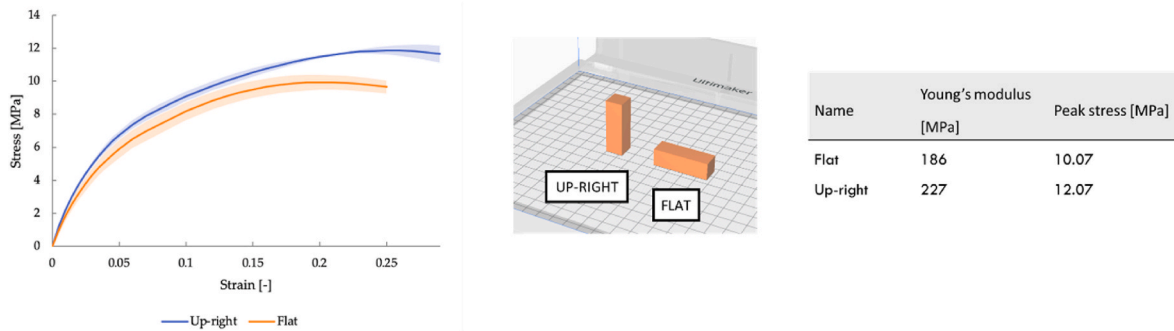


Fig. A1.4. Compression test results on the base material. For each configuration, the average Young's modulus and peak stress are reported. Three replicas are tested for each group.

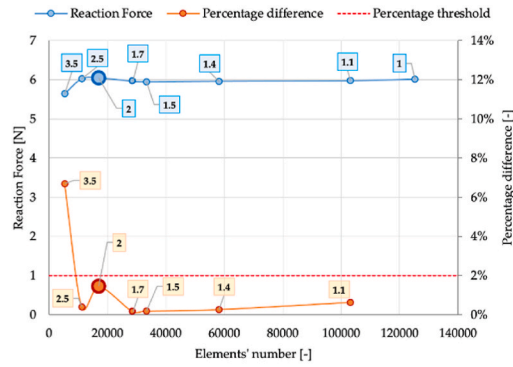
The samples from the *Up-right* configuration exhibited higher peak stress and Young's modulus, indicating this printing direction is preferable for structures under compression. This can be understood by considering the printed material as a composite: the material acts as fibers, while the adhesion between layers acts as the matrix. In the *Up-right* configuration, the fibers are perpendicular to the loading direction, maximizing material resistance. In contrast, the *Flat* configuration shares the load between the fibers and their adhesion, resulting in a less resistant structure.

Given that the bio-inspired structures and the reference cylinder for the quasi-static compressive tests are printed similarly to the *Up-right* configuration, the mean stress-strain curve from the three *Up-right* samples is used to define the material properties in numerical simulations.

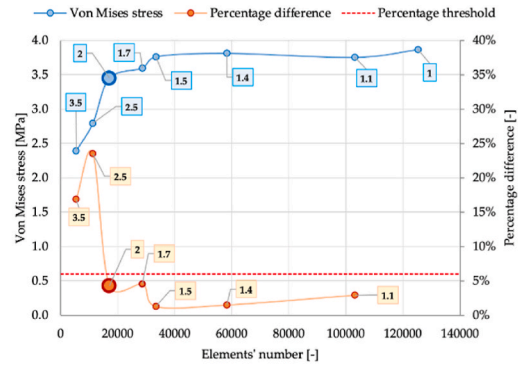
A.2 Mesh convergence analyses of the architected structures

Four-point bending mesh convergence

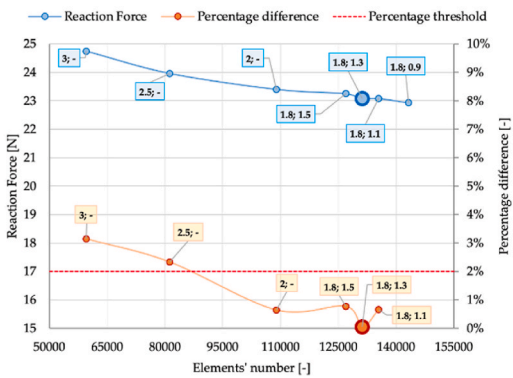
The convergence results for each structure are illustrated in Fig.A2.1, where Reaction Forces and Von Mises stress values are plotted with respect to the number of elements, with each point labeled according to the seed options set. In each graph, the selected mesh size is highlighted with a larger dot, and a dashed red line indicates the imposed threshold.



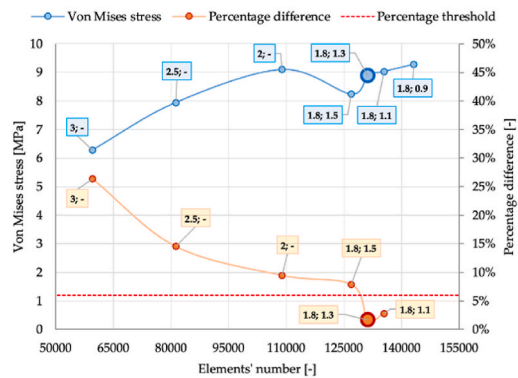
a) Reference cylinder, Reaction Force



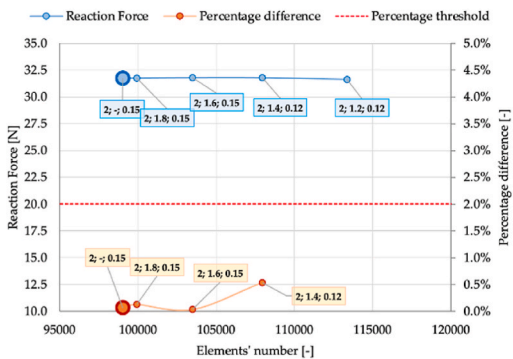
b) Reference cylinder, Von Mises stress



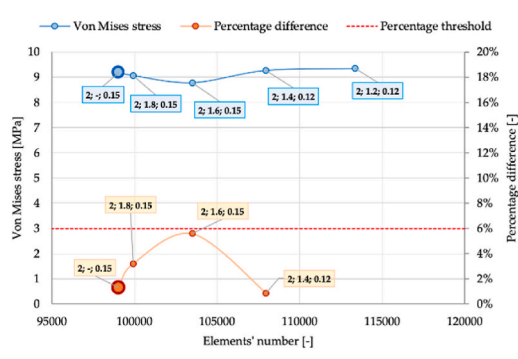
c) Horsetail structure, Reaction Force



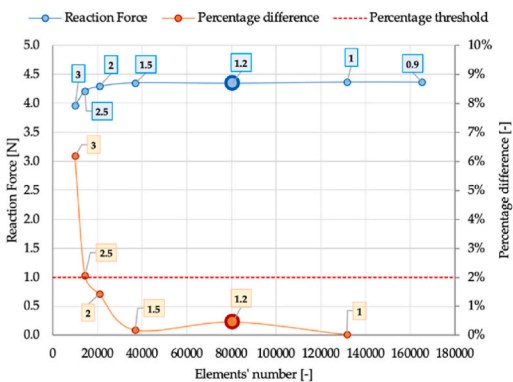
d) Horsetail structure, Von Mises stress



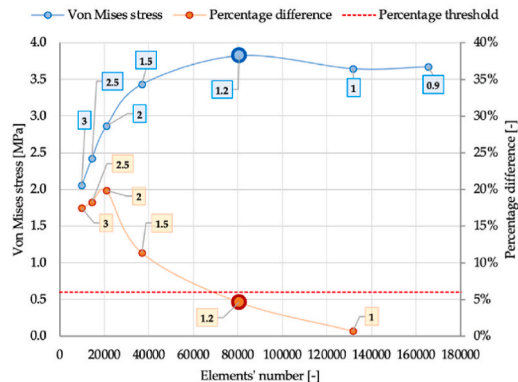
e) Bamboo Parenchyma structure, Reaction Force



f) Bamboo Parenchyma structure, Von Mises stress

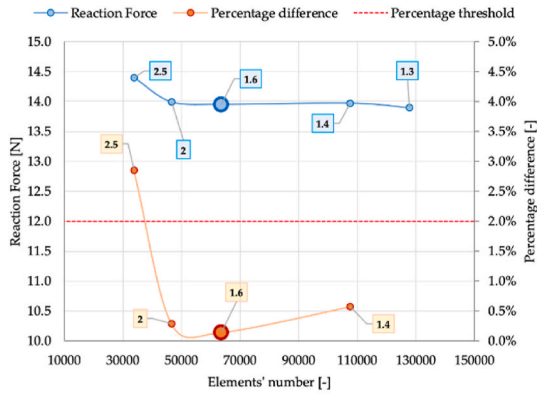


g) Bamboo Nodes structure, Reaction Force

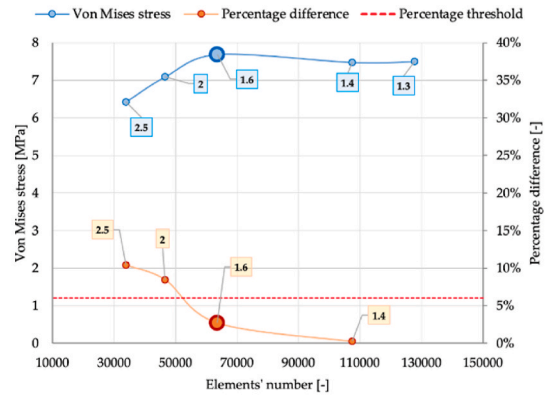


h) Bamboo Nodes structure, Von Mises stress

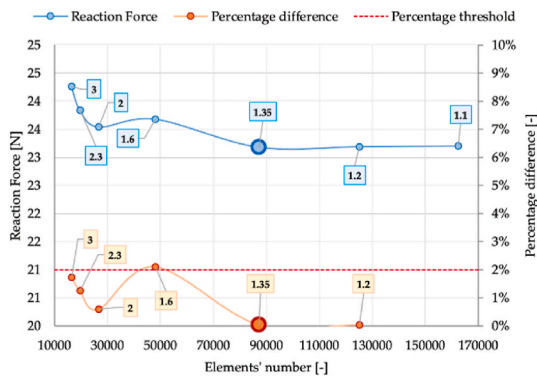
Fig. A2.1. Four-point bending test convergence analyses for the reference cylinder and all the bio-inspired configurations. The framed values are referred to the set seed size [mm].



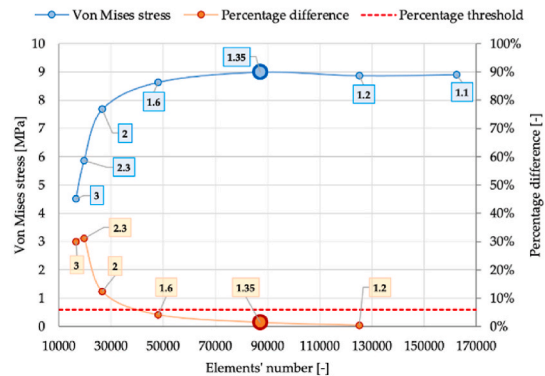
i) *Bouligand* structure, Reaction Force



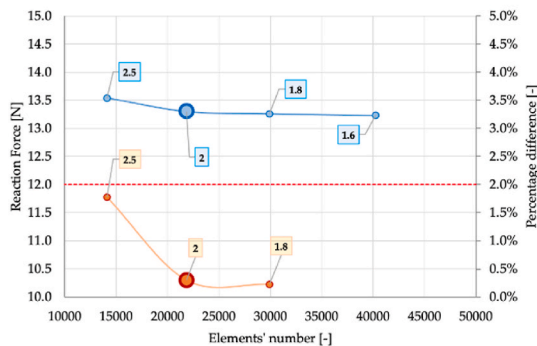
j) *Bouligand* structure, Von Mises stress



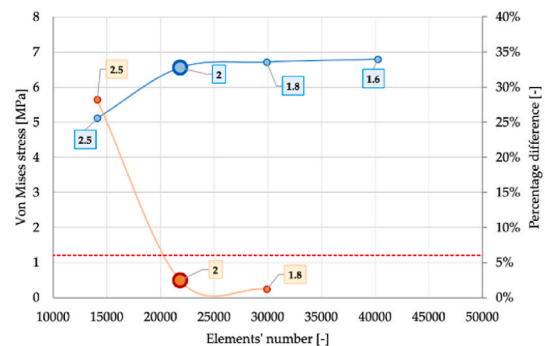
k) *Interlinks* structure, Reaction Force



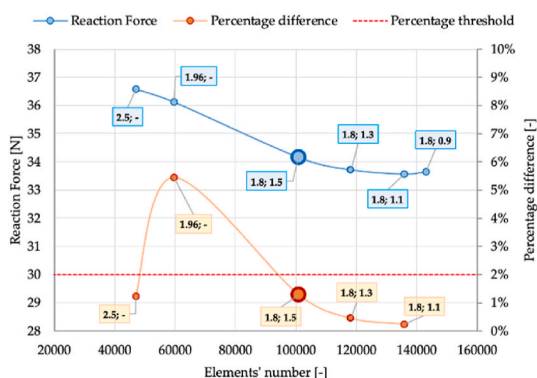
l) *Interlinks* structure, Von Mises stress



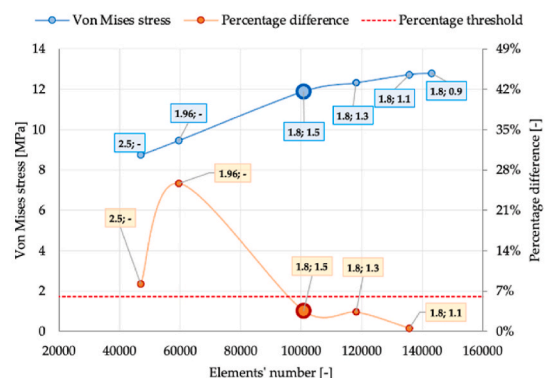
m) *Bamboo Bulkheads* structure, Reaction Force



n) *Bamboo Bulkheads* structure, Von Mises stress



o) *Intermediate* structure, Reaction Force



p) *Intermediate* structure, Von Mises stress

Fig. A2.1. (continued).

Due to their high element count, the *Horsetail*, *Bamboo Parenchyma*, *Intermediate*, and *Complete* structures receive particular attention. To prevent excessive computational cost and time, a strategy of mesh local refinement near the contact regions is employed. As a result, the total number of elements increases more slowly in these cases. [Table A2.1](#) summarizes all selected meshes and their relevant seed options.

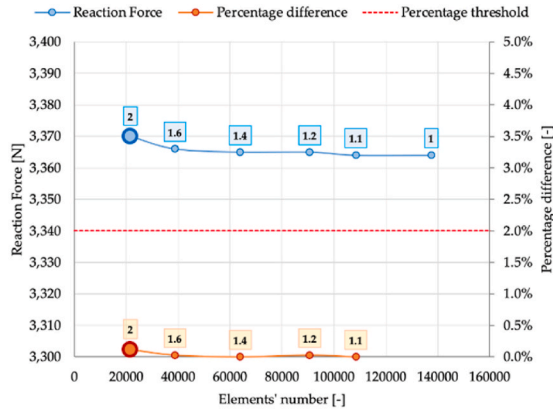
Table A2.1
Four-point bending numerical test resultant mesh parameters.

Structure	Global seeds		Local seeds
	Size [mm]	Curvature control [-]	Size [mm]
Reference cylinder	2.00	0.10	–
<i>Horsetail</i>	1.80	0.10	1.3
<i>Bamboo Parenchyma</i>	2.00	0.15	–
<i>Bamboo Nodes</i>	1.20	0.10	–
<i>Bouligand</i>	1.60	0.14	–
<i>Interlinks</i>	1.35	0.12	–
<i>Bamboo Bulkheads</i>	2.00	0.15	–
<i>Intermediate</i>	1.80	0.15	1.5

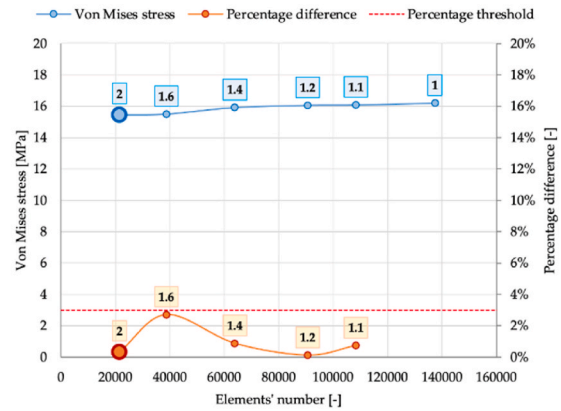
Compression mesh convergence analysis

Four convergence studies are performed for each structure tested in compression: the *Horsetail*, the *Bamboo Nodes*, the *Interlinks*, and the *Complete* structure.

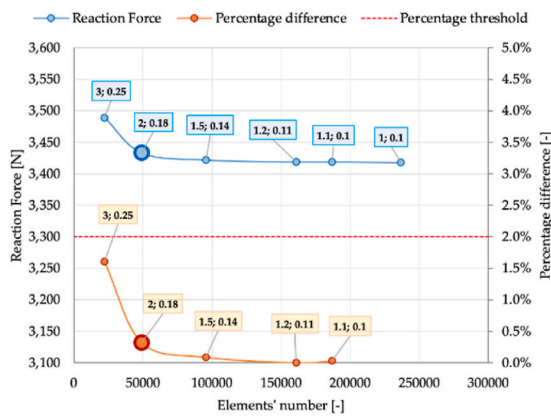
[Fig. A2.2](#) shows the convergence results for each structure, including both Reaction Forces and Von Mises stresses as functions of the number of elements. In each graph, the selected mesh size is highlighted by a larger dot, with the imposed threshold indicated by a dashed red line. The selected mesh parameters are listed in [Table A.2.2](#).



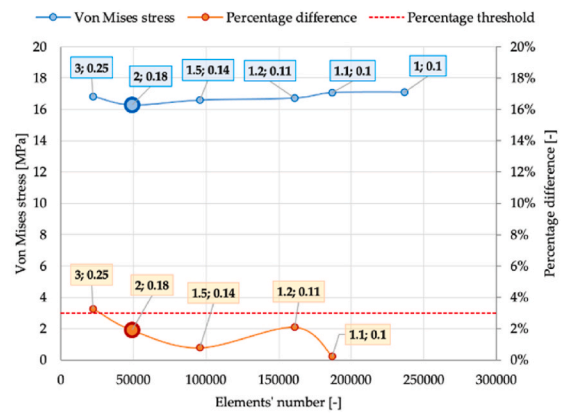
a) Reference cylinder, Reaction Force



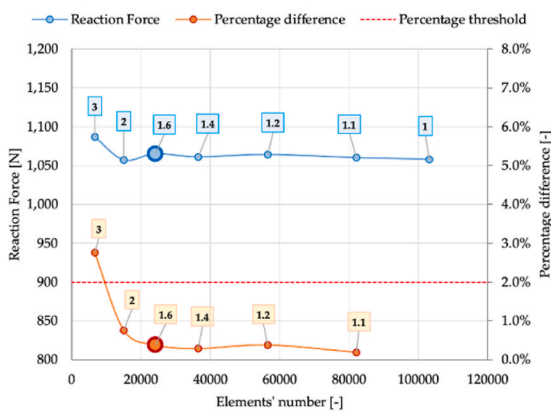
b) Reference cylinder, Von Mises stress



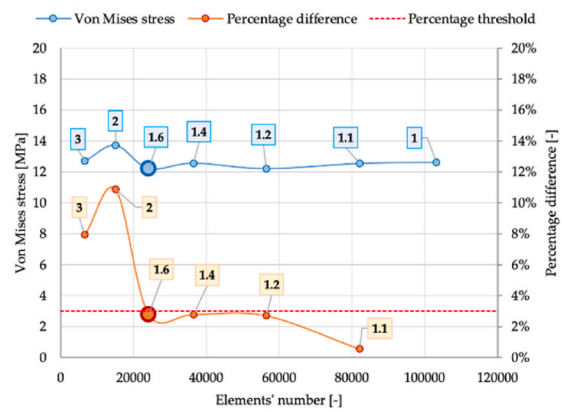
c) Horsetail structure, Reaction Force



d) Horsetail structure, Von Mises stress

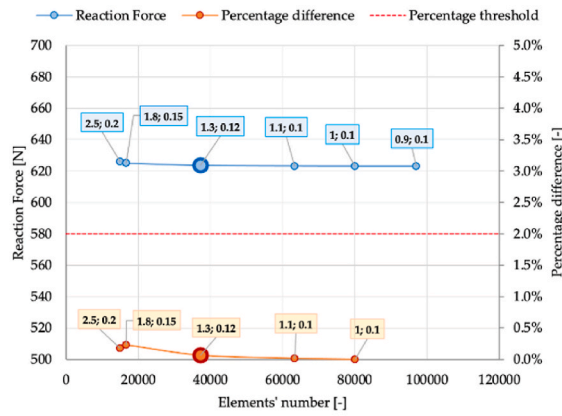


e) Bamboo Nodes structure, Reaction Force

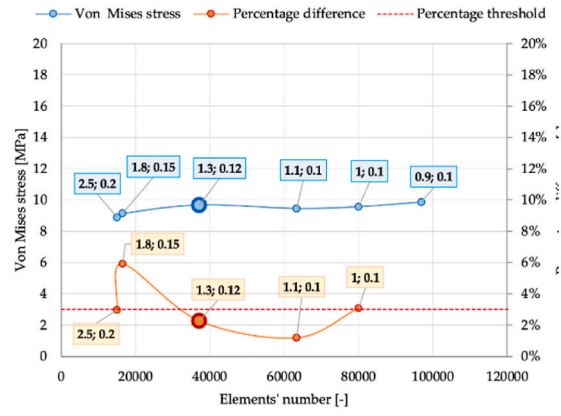


f) Bamboo Nodes structure, Von Mises stress

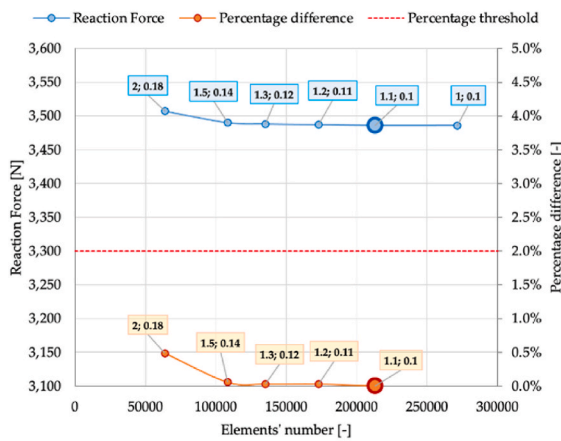
Fig. A2.2. Compression test convergency analyses. The framed values are referred to the seed size [mm] set.



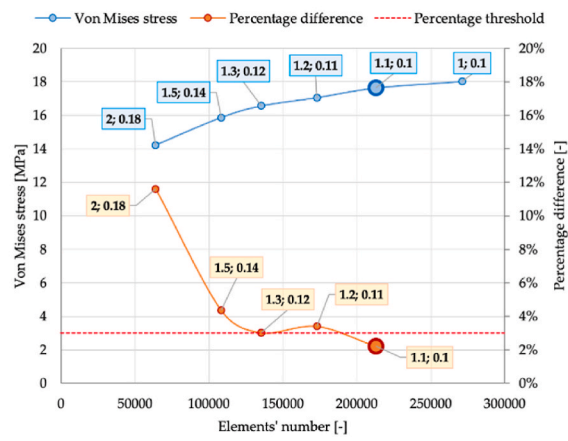
g) Interlinks structure, Reaction Force



h) Interlinks structure, Von Mises stress



i) Complete structure, Reaction Force



j) Complete structure, Von Mises stress

Fig. A2.2. (continued).

Table A2.2
Compression numerical test meshes' parameters.

Structure	Global seeds	
	Size [mm]	Curvature control [-]
Reference cylinder	2	0.1
Horsetail	2	0.18
Bamboo Nodes	1.6	0.1
Interlinks	1.3	0.12
Complete	1.1	0.1

Data availability

Data will be made available on request.

References

Amada, S., Ichikawa, Y., Munekata, T., Nagase, Y., Shimizu, H., 1997. Fiber texture and mechanical graded structure of bamboo. *Compos. Part B Eng.* 28, 13–20. [https://doi.org/10.1016/s1359-8368\(96\)00020-0](https://doi.org/10.1016/s1359-8368(96)00020-0).
 Bouligand, Y., 1972. Twisted fibrous arrangements in biological materials and cholesteric mesophases. *Tissue Cell* 4, 189–217. [https://doi.org/10.1016/S0040-8166\(72\)80042-9](https://doi.org/10.1016/S0040-8166(72)80042-9).
 Bru, J., Leite, M., Ribeiro, A.R., Reis, L., Deus, A.M., Fátima Vaz, M., 2020. Bioinspired structures for core sandwich composites produced by fused deposition modelling. *Proc. Inst. Mech. Eng. Part L J. Mater. Des. Appl.* 234, 379–393. <https://doi.org/10.1177/1464420719886906>.

Buccino, F., Aiazzi, I., Casto, A., Liu, B., Sbarra, M.C., Ziarelli, G., Vergani, L.M., Bagherifard, S., 2021a. Down to the bone: a novel bio-inspired design concept. *Materials* 14, 4226. <https://doi.org/10.3390/ma14154226>.
 Buccino, F., Martinoia, G., Vergani, L.M., 2021b. Torsion-resistant structures: a nature addressed solution. *Materials* 14, 5368. <https://doi.org/10.3390/ma14185368>.
 Buccino, F., Bruzzaniti, P., Candidori, S., Graziosi, S., Vergani, L.M., 2022a. Tailored torsion and bending-resistant avian-inspired structures. *Adv. Eng. Mater.* <https://doi.org/10.1002/adem.202200568>.
 Buccino, F., Bagherifard, S., D'Amico, L., Zagra, L., Banfi, G., Tromba, G., Vergani, L.M., 2022b. Assessing the intimate mechanobiological link between human bone micro-scale trabecular architecture and micro-damages. *Eng. Fract. Mech.* 270, 108582. <https://doi.org/10.1016/j.engfracmech.2022.108582>.
 Buccino, F., Bunt, A., Lazell, A., Vergani, L.M., 2022c. Mechanical design optimization of prosthetic hand's fingers: novel solutions towards weight reduction. *Materials* 15. <https://doi.org/10.3390/ma15072456>.
 Chen, J., Zhang, X., Okabe, Y., Saito, K., Guo, Z., Pan, L., 2017. The deformation mode and strengthening mechanism of compression in the beetle elytron plate. *Mater. Des.* 131, 481–486. <https://doi.org/10.1016/j.matdes.2017.06.014>.

- Chen, B.C., Zou, M., Liu, G.M., Song, J.F., Wang, H.X., 2018. Experimental study on energy absorption of bionic tubes inspired by bamboo structures under axial crushing. *Int. J. Impact Eng.* 115, 48–57. <https://doi.org/10.1016/j.ijimpeng.2018.01.005>.
- De Vivo Nicoloso, L.G., Pelz, J., Barrack, H., Kuester, F., 2021. Towards 3D printing of a monocoque transtibial prosthesis using a bio-inspired design workflow. *Rapid Prototyp. J.* 27, 67–80. <https://doi.org/10.1108/RPJ-06-2021-0136>.
- du Plessis, A., Broeckhoven, C., Yadroitsava, I., Yadroitsev, I., Hands, C.H., Kunju, R., Bhate, D., 2019. Beautiful and functional: a review of biomimetic design in additive manufacturing. *Addit. Manuf.* 27, 408–427. <https://doi.org/10.1016/j.ADDMA.2019.03.033>.
- Fayemi, P.E., Wanieck, K., Zollfrank, C., Maranzana, N., Aoussat, A., 2017. Biomimetics: process, tools and practice. *Bioinspiration Biomimetics* 12. <https://doi.org/10.1088/1748-3190/12/1/011002>.
- Gao, Q., Wang, L., Wang, Y., Wang, C., 2016. Crushing analysis and multiobjective crashworthiness optimization of foam-filled ellipse tubes under oblique impact loading. *Thin-Walled Struct.* 100, 105–112. <https://doi.org/10.1016/j.tws.2015.11.020>.
- Ginzburg, D., Pinto, F., Iervolino, O., Meo, M., 2017. Damage tolerance of bio-inspired helicoidal composites under low velocity impact. *Compos. Struct.* 161, 187–203. <https://doi.org/10.1016/j.compstruct.2016.10.097>.
- Ha, N.S., Pham, T.M., Chen, W., Hao, H., 2023. Energy absorption characteristics of bio-inspired hierarchical multi-cell bi-tubular tubes. *Int. J. Mech. Sci.* 251, 108260. <https://doi.org/10.1016/j.jjmeccsci.2023.108260>.
- Ha, N.S., Lee, T.U., Ma, J., Li, J., Xie, Y.M., 2024. Energy absorption of a bio-inspired cylindrical sandwich structure. *Thin-Walled Struct.* 195, 111378. <https://doi.org/10.1016/j.tws.2023.111378>.
- Katiyar, N.K., Goel, G., Hawi, S., Goel, S., 2021. Nature-inspired materials: emerging trends and prospects. *NPG Asia Mater.* 13, 1–16. <https://doi.org/10.1038/s41427-021-00322-y>.
- Khoshgoftar, M.J., Barkhordari, A., Limuti, M., Buccino, F., Vergani, L., Mirzaali, M.J., 2022. Bending analysis of sandwich panel composite with a re-entrant lattice core using zig-zag theory. *Sci. Rep.* 12, 1–12. <https://doi.org/10.1038/s41598-022-19930-x>.
- Li, D., Qin, R., Xu, J., Zhou, J., Chen, B., 2022. Topology optimization of thin-walled tubes filled with lattice structures. *Int. J. Mech. Sci.* 227, 107457. <https://doi.org/10.1016/j.jjmeccsci.2022.107457>.
- Libonati, F., Vergani, L., 2014. Bone toughness and crack propagation: an experimental study. *Procedia Eng.* 74, 464–467. <https://doi.org/10.1016/j.proeng.2014.06.298>.
- Libonati, F., Vellwock, A.E., El Louizi, F., Hoffmann, R., Colombo, C., Ziegmann, G., Vergani, L., 2020. Squeeze-winding: a new manufacturing route for biomimetic fiber-reinforced structures. *Compos. Part A Appl. Sci. Manuf.* 132, 105839. <https://doi.org/10.1016/j.compositesa.2020.105839>.
- Lindberg, A., Alfthan, J., Pettersson, H., Flodberg, G., Yang, L., 2018. Mechanical performance of polymer powder bed fused objects – FEM simulation and verification. *Addit. Manuf.* 24, 577–586. <https://doi.org/10.1016/j.addma.2018.10.009>.
- Maconachie, T., Leary, M., Lozanovski, B., Zhang, X., Qian, M., Faruque, O., Brandt, M., 2019. SLM lattice structures: properties, performance, applications and challenges. *Mater. Des.* 183. <https://doi.org/10.1016/j.matdes.2019.108137>.
- Mirzaali, M.J., Mussi, V., Vena, P., Libonati, F., Vergani, L., Strano, M., 2017. Mimicking the loading adaptation of bone microstructure with aluminum foams. *Mater. Des.* 126, 207–218. <https://doi.org/10.1016/j.matdes.2017.04.039>.
- Mirzaali, M.J., Libonati, F., Ferrario, D., Rinaudo, L., Messina, C., Olivieri, F.M., Cesana, B.M., Strano, M., Vergani, L., 2018. Determinants of bone damage: an ex vivo study on porcine vertebrae. *PLoS One* 13, e0202210. <https://doi.org/10.1371/journal.pone.0202210>.
- Mirzaali, M.J., Herranz de la Nava, A., Gunashekar, D., Nouri-Goushki, M., Veeger, R.P.E., Grossman, Q., Angeloni, L., Ghatkesar, M.K., Fratila-Apachitei, L.E., Ruffoni, D., Doubrovski, E.L., Zadpoor, A.A., 2020. Mechanics of bioinspired functionally graded soft-hard composites made by multi-material 3D printing. *Compos. Struct.* 237. <https://doi.org/10.1016/j.compstruct.2020.111867>.
- Mistry, Y., Weeger, O., Morankar, S., Shinde, M., Liu, S., Chawla, N., Chen, X., Penick, C. A., Bhate, D., 2023. Bio-inspired selective nodal decoupling for ultra-compliant interwoven lattices. *Commun. Mater.* 4, 1–8. <https://doi.org/10.1038/s43246-023-00363-6>, 2023.
- Moini, M., Olek, J., Youngblood, J.P., Magee, B., Zavattieri, P.D., 2018. Additive manufacturing and performance of architected cement-based materials. *Adv. Mater.* 30. <https://doi.org/10.1002/adma.201802123>.
- Morgan, D., Kucherenko, S., 2020. Comparing Option Pricing Methods in q, Wilmott 2020 58–69. <https://doi.org/10.1002/wilm.10876>.
- Mueller, J., Raney, J.R., Shea, K., Lewis, J.A., 2018. Architected lattices with high stiffness and toughness via multicore-shell 3D printing. *Adv. Mater.* 30. <https://doi.org/10.1002/adma.201705001>.
- Niknam, H., Akbarzadeh, A.H., 2020. Graded lattice structures: simultaneous enhancement in stiffness and energy absorption. *Mater. Des.* 196. <https://doi.org/10.1016/j.matdes.2020.109129>.
- Osorio, L., Trujillo, E., Lens, F., Ivens, J., Verpoest, I., Van Vuure, A.W., 2018. In-depth study of the microstructure of bamboo fibres and their relation to the mechanical properties. *J. Reinforc. Plast. Compos.* 37, 1099–1113. <https://doi.org/10.1177/0731684418783055>.
- Porter, M.M., Meraz, L., Calderon, A., Choi, H., Chouhan, A., Wang, L., Meyers, M.A., McKittrick, J., 2015. Torsional properties of helix-reinforced composites fabricated by magnetic freeze casting. *Compos. Struct.* 119, 174–184. <https://doi.org/10.1016/j.compstruct.2014.08.033>.
- Powelson, T., Yang, J., 2011. Prosthetics for transtibial amputees - a literature survey. *Proc. ASME Des. Eng. Tech. Conf.* 3, 753–764. <https://doi.org/10.1115/DETC2011-47024>.
- Qu, J., Lei, Y., Dong, Q., Wang, H., 2024. Hierarchical design of auxetic metamaterial with peanut-shaped perforations for extreme deformation: self-similar or not? *Eur. J. Mech. Solid.* 108, 105402. <https://doi.org/10.1016/j.EUROMECHSOL.2024.105402>.
- Ravi-Chandar, K., 2011. Design optimization and characterization of helicoidal composites with enhanced impact resistance. *Army Res. Off* 107. <http://www.dtic.mil/cgi-bin/GetTRDoc?Location=U2&doc=GetTRDoc.pdf&AD=ADA455390>.
- Renardy, M., Joslyn, L.R., Millar, J.A., Kirschner, D.E., 2021. To Sobol or not to Sobol? The effects of sampling schemes in systems biology applications. *Math. Biosci.* 337, 108593. <https://doi.org/10.1016/j.mbs.2021.108593>.
- Rohde, S., Cantrell, J., Jerez, A., Kroese, C., Damiani, D., Gurnani, R., DiSandro, L., Anton, J., Young, A., Steinbach, D., Ifju, P., 2018. Experimental characterization of the shear properties of 3D-printed ABS and polycarbonate parts. In: *Exp. Mech.* Springer, pp. 871–884. <https://doi.org/10.1007/s11340-017-0343-6>.
- Saldívar, M.C., Doubrovski, E.L., Mirzaali, M.J., Zadpoor, A.A., 2022. Nonlinear coarse-graining models for 3D printed multi-material biomimetic composites. *Addit. Manuf.* 58. <https://doi.org/10.1016/j.addma.2022.103062>.
- Saldívar, M.C., Tay, E., Isaakidou, A., Moosabeiki, V., Fratila-Apachitei, L.E., Doubrovski, E.L., Mirzaali, M.J., Zadpoor, A.A., 2023. Bioinspired rational design of bi-material 3D printed soft-hard interfaces. *Nat. Commun.* 14. <https://doi.org/10.1038/s41467-023-43422-9>.
- Shi, L., Nie, S., Tu, F., 2024. Mechanical properties of lotus petiole bio-inspired structures under quasi-static radial load. *Eur. J. Mech. Solid.* 107, 105396. <https://doi.org/10.1016/j.EUROMECHSOL.2024.105396>.
- Sullivan, T.N., Wang, B., Espinosa, H.D., Meyers, M.A., 2017. Extreme lightweight structures: avian feathers and bones. *Mater. Today* 20, 377–391. <https://doi.org/10.1016/j.mattod.2017.02.004>.
- Svatík, J., Lepcio, P., Ondreaš, F., Zárýbnická, K., Zbončák, M., Menčík, P., Jančár, J., 2021. PLA toughening via bamboo-inspired 3D printed structural design. *Polym. Test.* 104. <https://doi.org/10.1016/j.polymertesting.2021.107405>.
- Tan, T., Rahbar, N., Allameh, S.M., Kwofie, S., Dissmore, D., Ghavami, K., Soboyejo, W. O., 2011. Mechanical properties of functionally graded hierarchical bamboo structures. *Acta Biomater.* 7, 3796–3803. <https://doi.org/10.1016/j.actbio.2011.06.008>.
- Tavangarian, F., Proano, C., Zolko, C., 2019. Performance of low-cost 3D printed pylon in lower limb prosthetic device. *Miner. Met. Mater. Ser.* 1207–1215. https://doi.org/10.1007/978-3-030-05861-6_115.
- Taylor, D., Kinane, B., Sweeney, C., Sweetnam, D., O'Reilly, P., Duan, K., 2015. The biomechanics of bamboo: investigating the role of the nodes. *Wood Sci. Technol.* 49, 345–357. <https://doi.org/10.1007/s00226-014-0694-4>.
- Tran, P., Ngo, T.D., Ghazlan, A., Hui, D., 2017. Bimaterial 3D printing and numerical analysis of bio-inspired composite structures under in-plane and transverse loadings. *Compos. Part B Eng.* 108, 210–223. <https://doi.org/10.1016/j.compositesb.2016.09.083>.
- Ultimaker, ultimaker PP technical datasheet. <https://ultimaker.com/materials/>, 2022.
- Umer, R., Balawi, S., Raja, P., Cantwell, W.J., 2014. The energy-absorbing characteristics of polymer foams reinforced with bamboo tubes. *J. Sandw. Struct. Mater.* 16, 108–122. <https://doi.org/10.1177/1099636213509644>.
- Wang, X., Li, D., 2020. A new biomimetic composite structure with tunable stiffness and superior toughness via designed structure breakage. *Materials* 13, 636. <https://doi.org/10.3390/ma13030636>.
- Wegst, U.G.K., 2011. Bending efficiency through property gradients in bamboo, palm, and wood-based composites. *J. Mech. Behav. Biomed. Mater.* 4, 744–755. <https://doi.org/10.1016/j.jmbm.2011.02.013>.
- Wegst, U.G.K., Ashby, M.F., 2004. The mechanical efficiency of natural materials. *Philos. Mag.* 84, 2167–2186. <https://doi.org/10.1080/14786430410001680935>.
- Xiao, Y., Yin, H., Fang, H., Wen, G., 2016. Crashworthiness design of horsetail-bionic thin-walled structures under axial dynamic loading. *Int. J. Mech. Mater. Des.* 12, 563–576. <https://doi.org/10.1007/s10999-016-9341-6>.
- Xiong, Y., Yang, H., Li, X., Lei, H., Lu, G., 2023. Crashworthy optimization of skeleton-filled FRP tubes based on back propagation neural network. *Heliyon* 9, e23019. <https://doi.org/10.1016/j.heliyon.2023.E23019>.
- Yaraghi, N.A., Guarín-Zapata, N., Grunenfelder, L.K., Hintsala, E., Bhowmick, S., Hiller, J.M., Betts, M., Principe, E.L., Jung, J.Y., Sheppard, L., Wuhler, R., McKittrick, J., Zavattieri, P.D., Kisailus, D., A Sinusoidally Architected Helicoidal BioComposite, 2016. *Adv. Mater.* 28, 6835–6844. <https://doi.org/10.1002/adma.201600786>.
- Yin, H., Xiao, Y., Wen, G., Qing, Q., Wu, X., 2015. Crushing analysis and multi-objective optimization design for bionic thin-walled structure. *Mater. Des.* 87, 825–834. <https://doi.org/10.1016/j.matdes.2015.08.095>.

- Yin, H., Xiao, Y., Wen, G., Gan, N., Chen, C., Dai, J., 2016. Multi-objective robust optimization of foam-filled bionic thin-walled structures. *Thin-Walled Struct.* 109, 332–343. <https://doi.org/10.1016/j.tws.2016.10.011>.
- Yin, S., Chen, H., Li, J., Yu, T.X., Xu, J., 2019. Effects of architecture level on mechanical properties of hierarchical lattice materials. *Int. J. Mech. Sci.* 157–158, 282–292. <https://doi.org/10.1016/j.ijmecsci.2019.04.051>.
- Zappa, G., Cocchi, L., Candidori, S., Buccino, F., Vergani, L., Graziosi, S., 2024. Twinning-inspired hexagonal close-packed metamaterials for enhanced energy absorption. *Mater. Des.*, 113098 <https://doi.org/10.1016/J.MATDES.2024.113098>.
- Zheng, B., Liu, Y., Liu, J., Yin, S., Xu, J., 2019. Novel mechanical behaviors of DNA-inspired helical structures with chirality. *Int. J. Mech. Sci.* 161–162. <https://doi.org/10.1016/j.ijmecsci.2019.105025>.
- Zhou, H., Zhong, Y., Lan, J., Lu, W., Deng, X., Huang, J., 2024. Crashworthiness analysis of novel bidirectional gradient hierarchical double tubes inspired by the leaf tissue. *Eur. J. Mech. Solid.* 107, 105391. <https://doi.org/10.1016/J.EUROMECHSOL.2024.105391>.